

Reconsidering the nonlinear emergent inductance: time-varying Joule heating and its impact on the AC electrical response

Soju Furuta,¹ Wataru Koshibae,² Keisuke Matsuura,¹ Nobuyuki Abe,³ Fei
Wang,⁴ Shuyun Zhou,⁴ Taka-hisa Arima,^{2,5} and Fumitaka Kagawa^{1,2,*}

¹*Department of Physics, Tokyo Institute of Technology, Tokyo 152-8551, Japan*

²*RIKEN Center for Emergent Matter Science (CEMS), Wako 351-0198, Japan*

³*Department of Physics, College of Humanities and Sciences,
Nihon University, Tokyo 156-8550, Japan*

⁴*Department of Physics, Tsinghua University,
Beijing 100084, People's Republic of China*

⁵*Department of Advanced Materials Science,
University of Tokyo, Kashiwa 277-8561, Japan*

(Dated: July 2, 2024)

Abstract

A nonlinearly enhanced electrical reactance, $\text{Im } Z$, under a large AC current has been measured to explore emergent inductors, which constitute a new class of inductors based on the spin-transfer torque effect. A nonlinear $\text{Im } Z$ has been observed in conducting magnets that contain noncollinear spin textures and interpreted as the realization of an inductance due to current-induced spin dynamics. However, curious behavior has concomitantly been observed. For instance, the nonlinear $\text{Im } Z$ always has a cutoff frequency of 10^0 – 10^4 Hz, which is much lower than the resonance frequency of a ferromagnetic domain wall, $\sim 10^7$ Hz; furthermore, the temperature and magnetic field variations in $\text{Im } Z$ appear to be considerably correlated with those in the temperature derivative of resistance. This behavior appears to be difficult to understand in terms of the current-induced spin dynamics, and therefore, the earlier interpretation of the nonlinear $\text{Im } Z$ should be further verified. Here, we theoretically and experimentally show that time-varying Joule heating and its impact on the AC electrical response can naturally explain these observations. In the experimental approach, we study the nonlinear AC electrical response of two conducting materials that exhibit no magnetic order, CuIr_2S_4 and $1T'$ - MoTe_2 . Under time-varying Joule heating, a nonlinearly enhanced $\text{Im } Z$ with the curious behavior mentioned above is observed in both systems. Our study implies that the nonlinear $\text{Im } Z$ previously observed in noncollinear magnets includes a considerable contribution of the Joule-heating-induced apparent AC impedance.

I. INTRODUCTION

The exchange of spin angular momentum between flowing conduction electrons and an underlying magnetic texture leads to the spin-transfer-torque (STT) effect on the magnetic texture [1, 2]. Nagaosa theoretically proposed a new class of inductors arising from the STT-induced elastic deformation of noncollinear magnetic textures [3], and these inductors are now referred to emergent inductors. The time evolution of a magnetic texture brings about an emergent electric field (EEF) [4, 5]. Under an AC electric current below the threshold value, the magnetic texture remains in the pinned regime [6–14] and is periodically deformed, giving rise to a time-varying effective U(1) gauge field and thus an oscillating EEF. From an energetic perspective, an emergent inductor stores energy in a magnetic texture under a current [15], in contrast to classical inductors, which store energy as the magnetic field under a current [16].

Soon after the theoretical proposal of emergent inductors [3], experimental studies were launched. The AC impedance $Z(\omega)$, also termed complex resistivity $\rho(\omega)$ (normalized with the sample dimensions), where ω represents the angular frequency, was extensively investigated for materials that contain a noncollinear magnetic texture [17–20]. Thus far, the imaginary part of the complex resistivity of such magnetic materials divided by ω , i.e., $\text{Im } \rho^{1\omega}(\omega, j_0)/\omega$, has been commonly found to be negligibly small for a weak AC current density, $j_0 e^{i\omega t}$, whereas it is significantly enhanced and becomes detectable for a relatively large AC current density, $j_0 \sim 10^8 \text{ A m}^{-2}$; here, the complex $\rho^{1\omega}(\omega, j_0)$ is not differential resistivity but defined by the 1ω Fourier component of the time-varying electric field under $j_0 e^{i\omega t}$ divided by j_0 . The nonlinearly enhanced $\text{Im } \rho^{1\omega}(\omega, j_0)/\omega$ has been interpreted as emergent inductance. The present authors believe, however, that this interpretation needs to be reconsidered; in particular, several observations seem to be not well explained within the EEF-based inductance scenario. Below, we raise fundamental questions associated with the interpretation.

Question I. The values of $\text{Im } \rho^{1\omega}(j_0, \omega)/\omega$ reported in experiments [17–20] appear too large to be ascribed to the EEF origin. Linear-response EEF theory includes \hbar and predicts only a small value of $\text{Im } \rho^{1\omega}(\omega)/\omega$, on the order of 10^{-11} – $10^{-13} \mu\Omega \text{ cm s}$ [3, 15]. Contrastingly, the magnitudes of experimentally observed $\text{Im } \rho^{1\omega}(\omega, j_0)/\omega$ at low ω are $\approx -9 \times 10^{-7} \mu\Omega \text{ cm s}$ for $\text{Gd}_3\text{Ru}_4\text{Al}_{12}$ [17], $\approx -4 \times 10^{-4} \mu\Omega \text{ cm s}$ for YMn_6Sn_6 [18], and $\approx -3 \times 10^{-3} \mu\Omega \text{ cm s}$ for

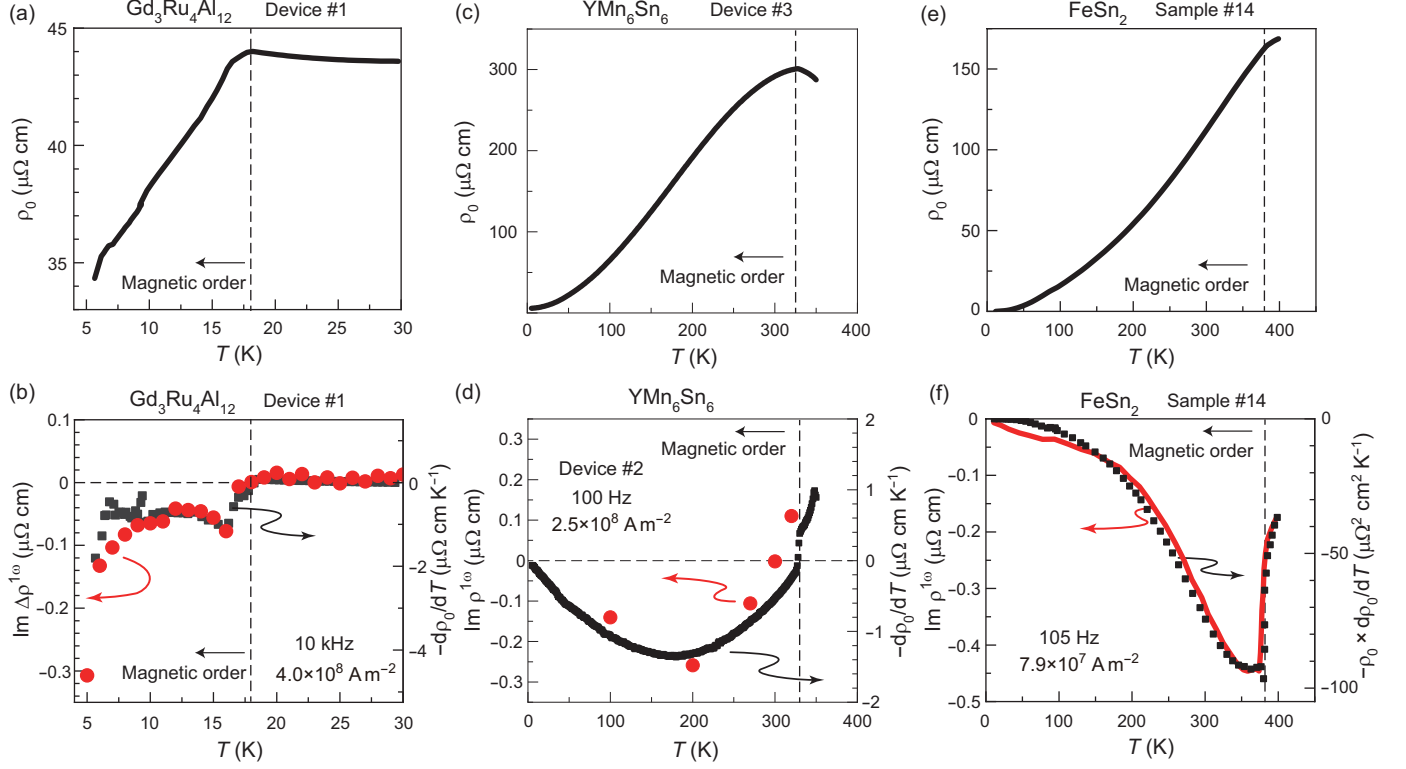


FIG. 1. Correlation between nonlinear $\text{Im } \rho(j_0)$ and $-\text{d}\rho_0/\text{d}T$ in the reported data. (a, b) ρ_0 - T profile (a) and $\text{Im } \Delta\rho^{1\omega}(j_0)$ - T and $(-\text{d}\rho_0/\text{d}T)$ - T profiles (b) of $\text{Gd}_3\text{Ru}_4\text{Al}_{12}$. (c, d) ρ_0 - T profile (c) and $\text{Im } \rho^{1\omega}(j_0)$ - T and $(-\text{d}\rho_0/\text{d}T)$ - T profiles (d) of YMn_6Sn_6 . (e, f) ρ_0 - T profile (e) and $\text{Im } \rho^{1\omega}$ - T and $(-\rho_0 \times \text{d}\rho_0/\text{d}T)$ - T profiles (f) of FeSn_2 . The ρ_0 - T and $\text{Im } \rho^{1\omega}(j_0)$ - T profiles were taken from the literature [17–19], and we constructed the $(-\text{d}\rho_0/\text{d}T)$ - T profiles from the data. Note that for YMn_6Sn_6 , the $\text{Im } \rho^{1\omega}(j_0)$ - T and $(-\text{d}\rho_0/\text{d}T)$ - T profiles were collected from different devices.

FeSn_2 [19] for $j_0 \sim 10^8 \text{ A m}^{-2}$. Although the experimental reports emphasize that these values are observed in the nonlinear regime, understanding such gigantic responses within the EEF framework is nontrivial even if the EEF beyond the linear-response regime is considered. Furthermore, the sign of the reported $\text{Im } \rho^{1\omega}(\omega, j_0)$ is negative in most cases. The negative $\text{Im } \rho^{1\omega}(\omega, j_0)/\omega$ was interpreted as the inductance being negative, but the theory of dynamical systems concludes that unstable behavior occurs when the coefficient of the time derivative of the electric current, $\text{d}I/\text{d}t$, is negative [21] (for details, see Supplementary Materials [22]).

Question II. The ω dependence of the nonlinear $\text{Im } \rho^{1\omega}(\omega, j_0)/\omega$ reported thus far exhibits a cutoff frequency as low as $\sim 10^3$ – 10^4 Hz for micrometer-sized fabricated specimens [17, 18]

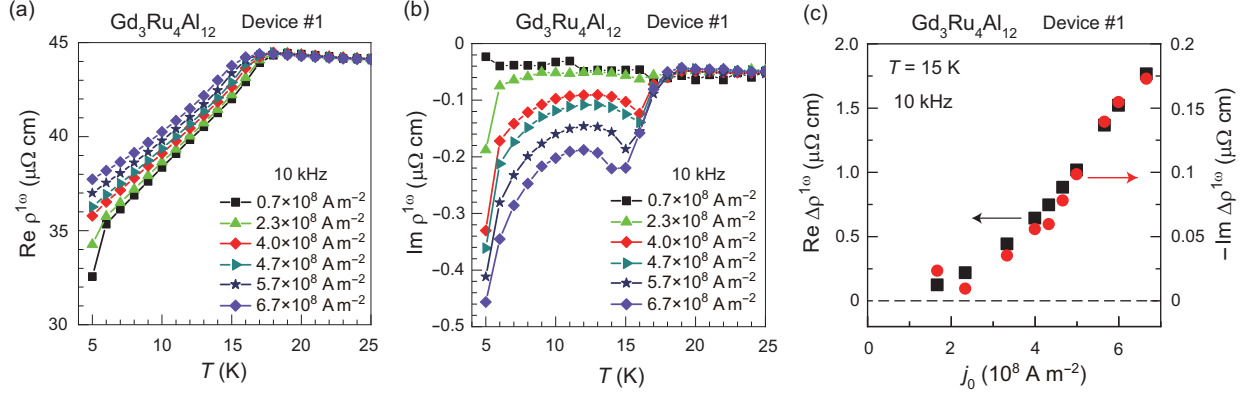


FIG. 2. Nonlinear $\rho^{1\omega}$ in $\text{Gd}_3\text{Ru}_4\text{Al}_{12}$. (a, b) $\text{Re } \rho^{1\omega}-T$ (a) and $\text{Im } \rho^{1\omega}-T$ (b) profiles under various AC current densities, $j_0 \sin \omega t$, at $\omega/(2\pi) = 10$ kHz. (c) Current-density dependence of complex $\Delta\rho^{1\omega}(j_0) = \rho^{1\omega}(j_0) - \rho^{1\omega}(0.7 \times 10^8 \text{ A m}^{-2})$ at 15 K. The panels are constructed from the raw data published in the literature [17].

and $\sim 10^2$ Hz for needle-like bulk crystals [19]. These results were interpreted as indicating that the spin texture under consideration has slow dynamics, but the experimentally found resonance frequency of a ferromagnetic domain wall of $\sim 10^7$ Hz should be noted [23]. Currently, there is no understanding of why such extremely slow dynamics are ubiquitously observed in the study of nonlinear emergent inductance.

Question III. By inspecting the previous reports [17–19], we find a possible correlation between the nonlinearly enhanced $\text{Im } \rho^{1\omega}(\omega, j_0)$ and the temperature (T) derivative of the linear-response DC resistivity ρ_0 . As summarized in Fig. 1, the $\text{Im } \Delta\rho^{1\omega}(\omega, j_0)-T$ profile appears similar to the $(-d\rho_0/dT)-T$ profile for $\text{Gd}_3\text{Ru}_4\text{Al}_{12}$ [Figs. 1(a) and (b)] [17] and YMn_6Sn_6 [Figs. 1(c) and (d)] [18] or to the $(-\rho_0 \times d\rho_0/dT)-T$ profile for FeSn_2 [Figs. 1(e) and (f)] [19]. In particular, regarding $\text{Gd}_3\text{Ru}_4\text{Al}_{12}$, we could construct the approximate $d\rho_0/dT-H$ profile (H denotes the magnetic field) and compare this with the $\text{Im } \rho^{1\omega}-H$ profile (not the $\text{Im } \Delta\rho^{1\omega}-H$ profile because of the lack of linear-response data), as shown in Figs. 8(a)–(c) in the APPENDIX. Remarkably, the complicated H dependence shown in $\text{Im } \rho^{1\omega}$ is reproduced by the H -dependent $-d\rho_0/dT$ at least qualitatively, thereby indicating that a considerable correlation exists between $\text{Im } \rho^{1\omega}$ and $-d\rho_0/dT$. This propensity seems difficult to understand in terms of the EEF, which is determined by the spin dynamics and does not involve the T derivative of the scattering rate.

In exploring clues to answer questions I–III, we realize that the magnitude of the non-

linear enhancement of $\text{Re } \rho^{1\omega}(\omega, j_0)$ is larger than that of $\text{Im } \rho^{1\omega}(\omega, j_0)$; i.e., regarding the nonlinear part, $\text{Re } \Delta\rho^{1\omega} > \text{Im } \Delta\rho^{1\omega}$ holds, where $\Delta\rho^{1\omega}(\omega, j_0) \equiv \rho^{1\omega}(\omega, j_0) - \rho_0(\omega)$, with $\rho_0(\omega)$ representing a linear-response complex value. For $\text{Gd}_3\text{Ru}_4\text{Al}_{12}$, for instance, the j_0 -dependent $\text{Re } \rho^{1\omega}(j_0)\text{-}T$ and $\text{Im } \rho^{1\omega}(j_0)\text{-}T$ profiles in Figs. 2(a) and (b), respectively, were reported [17]. The simple temperature shift cannot explain the pronounced variations in $\text{Im } \rho^{1\omega}(j_0)$ at 10 kHz, and on this basis, the nonlinear $\text{Im } \rho^{1\omega}(j_0)$ was interpreted as originating from the current-induced EEF. However, the nonlinear part, which is here defined as $\Delta\rho^{1\omega}(j_0) \equiv \rho^{1\omega}(j_0) - \rho^{1\omega}(0.7 \times 10^8 \text{ A m}^{-2})$, exhibits a $\text{Re } \Delta\rho^{1\omega}$ that is approximately 10 times larger than $\text{Im } \Delta\rho^{1\omega}$ for all j_0 values [Fig. 2(c)]. $\text{Re } \rho \gg \text{Im } \rho$ at low ω is a characteristic of dissipative responses of a resistor, and therefore, regarding the $\text{Im } \Delta\rho^{1\omega}(j_0)$ under an AC current as a delayed response of $\text{Re } \Delta\rho^{1\omega}(j_0)$ appears more reasonable. In contrast, the nonlinear inductance mechanism discussed in previous studies assumes that the nonlinearity occurs mainly in the imaginary part; i.e., $\text{Im } \Delta\rho^{1\omega} \gg \text{Re } \Delta\rho^{1\omega}$ at low ω , which is a characteristic of nondissipative responses of an inductor and inconsistent with the behavior shown in Fig. 2(c).

These unresolved or hitherto overlooked issues led us to reconsider the origin of the nonlinear $\text{Im } \Delta\rho^{1\omega}$ observed in previous experiments. In particular, on the basis of Figs. 1 and 2, we explored a dissipative mechanism. In general, when nonlinear electrical responses under a large current are examined, the impact of Joule heating must be considered. In AC impedance measurements, the sample temperature is time-varying with a 2ω modulation as a result of the time-varying current, and thus, the situation is more complicated than DC measurements, in which Joule heating only results in a static temperature increase. Such time-varying heating may induce a nonlinear $\text{Im } \Delta\rho^{1\omega}$. While its impact has been discussed in the context of detecting a superconducting transition [24], to the best of the authors' knowledge, the impact of time-varying Joule heating on the nonlinearly enhanced $\text{Im } \rho^{1\omega}$ has not been discussed in the experimental studies on emergent inductance. This motivated us to scrutinize whether the nonlinear $\text{Im } \rho^{1\omega}$ caused by AC Joule heating is truly negligible in the reported nonlinear emergent inductance.

II. JOULE HEATING MODEL FOR THE NONLINEAR AC ELECTRICAL RESPONSE

A. Model construction

Below, we aim to clarify $\rho(\omega, j_0)$ characteristics when a large AC current is applied to the sample such that the effect of time-varying Joule heating is not negligible; that is, we consider a sample in contact with a heat bath of temperature T_0 and derive the voltage responses under the time-varying sample temperature due to Joule heating. For simplicity, we neglect the temperature gradient within the sample. To analytically solve this problem, we make the following assumptions that appear to be physically reasonable.

Assumption #1. The instantaneous voltage drop in the time-varying self-heated sample is given by:

$$V(t) = R_0(T(t))I(t), \quad (1)$$

where $R_0(T)$ denotes the linear-response resistance at T . In this model, only this resistive mechanism is considered for the relationship between the voltage and current. In other words, neither inductive nor capacitive mechanisms are considered.

Assumption #2. We treat the temperature increase of the sample, $\Delta T(t) = T(t) - T_0$, with respect to the AC power input with angular frequency Ω , $P(t) = \text{Re}(P_0 e^{i\Omega t})$, as being within the linear-response regime. This means that we consider the lowest-order nonlinear response to the AC current input. By introducing a complex response function, $\chi^*(\Omega, T_0) = \chi'(\Omega, T_0) - i\chi''(\Omega, T_0)$, $\Delta T(t)$ is given by:

$$\begin{aligned} \Delta T(t) &= \text{Re}[\chi^*(\Omega, T_0)P_0 e^{i\Omega t}] \\ &= P_0[\chi'(\Omega, T_0) \cos \Omega t + \chi''(\Omega, T_0) \sin \Omega t], \end{aligned} \quad (2)$$

which is the expression for a cosine-wave power input, $P(t) = P_0 \cos \Omega t$. By definition, in the DC limit, $\chi'(\Omega, T_0)$ approaches a finite value, $\chi_0(T_0)$, and $\chi''(\Omega, T_0)$ approaches zero; i.e., we impose $\lim_{\Omega \rightarrow 0} \chi'(\Omega, T_0) = \chi_0(T_0)$ and $\lim_{\Omega \rightarrow 0} \chi''(\Omega, T_0) = 0$. Note that χ^* is determined by the heat capacitance of the system and the heat conduction to the heat bath; thus, χ^* depends on the volume and geometry of the sample, the details of the thermal contacts, etc.

Assumption #3. A system has a nonzero thermal-response time, $\tau_{\text{therm}} (> 0)$, which is a phenomenon known as thermal relaxation. Thus, under an AC power input, the thermal

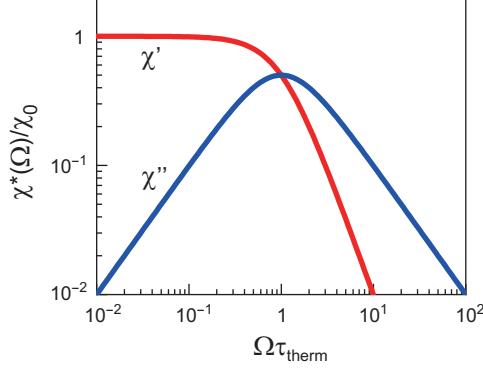


FIG. 3. Example of the response function, $\chi^*(\Omega) = \chi' - i\chi''$, of the temperature change in response to the power input. The functional form of Eq. (3) with $\alpha = 0$ is displayed on a double logarithmic scale.

response of the sample is more or less delayed (i.e., $\chi'' > 0$), and correspondingly, $\chi^*(\Omega, T_0)$ has a Ω dependence with a cutoff frequency of $\approx 1/(2\pi\tau_{\text{therm}})$. The form of $\chi^*(\Omega)$ can be approximately captured by a polydispersive Cole-Cole-type response:

$$\chi^*(\Omega, T) = \frac{\chi_0(T)}{1 + (i\Omega\tau_{\text{therm}}(T))^{1-\alpha}}, \quad (3)$$

where α represents the polydispersivity. For the readers' reference, we display the functional form of Eq. (3) for the case of a monodispersive relaxation, $\alpha = 0$, in Fig. 3. The details of χ^* depend on the system as mentioned above. Nevertheless, the only important feature in the following discussion is that $\chi^*(\Omega, T_0)$ has a cutoff frequency determined by the thermal-response dynamics and satisfies $\lim_{\Omega \rightarrow 0} \chi'(\Omega, T_0) = \chi_0(T_0)$ and $\lim_{\Omega \rightarrow 0} \chi''(\Omega, T_0) = 0$. Equation (3) is an example of a function that satisfies these characteristics.

Assumption #4. $\Delta T(t)$ is so small that the time-dependent resistance, $R(T(t))$, is well approximated by:

$$\begin{aligned} R(T(t)) &= R_0(T_0) + \Delta R_0(\Delta T(t)) \\ &\approx R_0(T_0) + \frac{dR_0(T_0)}{dT} \Delta T(t), \end{aligned} \quad (4)$$

where $dR_0(T_0)/dT \equiv dR_0/dT|_{T=T_0}$.

B. Derivation of the nonlinear AC electrical response

With the above assumptions, one can analytically derive $P(t)$, $\Delta T(t)$, $R(t)$, and, finally, $V(t)$ in sequence. We consider the situation in which a sine-wave AC current with angular frequency ω , $I(t) = I_0 \sin \omega t$, is applied to the sample. Hence, the time-varying power input, $P(t)$, is given by:

$$\begin{aligned} P(t) &\approx R_{2\text{probe}}(T_0)(I_0 \sin \omega t)^2 \\ &= P_0 \frac{1 - \cos 2\omega t}{2} \\ &= \frac{P_0}{2} - \frac{P_0}{2} \text{Re}(e^{i2\omega t}), \end{aligned} \quad (5)$$

where $R_{2\text{probe}}$ denotes the two-probe resistance including the contact resistance R_{contact} and $P_0(I_0) \equiv R_{2\text{probe}}(T_0)I_0^2 = (R_0(T_0) + R_{\text{contact}}(T_0))I_0^2$. Here, we neglect the deviation from Eq. (5) due to the time-varying two-probe resistance. By combining this result with Eq. (2) and further considering Eqs. (4) and (1) in sequence, one obtains:

$$\begin{aligned} \Delta T(t) &\approx \frac{\chi_0(T_0)P_0}{2} - \frac{P_0}{2} \text{Re}[\chi^*(2\omega, T_0)e^{i2\omega t}] \\ &= \frac{\chi_0(T_0)P_0}{2} - \frac{P_0}{2} [\chi'(2\omega, T_0) \cos 2\omega t + \chi''(2\omega, T_0) \sin 2\omega t]. \\ \therefore R(t) &\approx R_0(T_0) + \frac{dR_0(T_0)}{dT} \left\{ \frac{\chi_0(T_0)P_0}{2} - \frac{P_0}{2} [\chi'(2\omega, T_0) \cos 2\omega t + \chi''(2\omega, T_0) \sin 2\omega t] \right\}. \\ \therefore V(t) &\approx R_0(T_0)I_0 \sin \omega t \\ &\quad + \frac{dR_0(T_0)}{dT} \left\{ \frac{\chi_0(T_0)P_0}{2} - \frac{P_0}{2} [\chi'(2\omega, T_0) \cos 2\omega t + \chi''(2\omega, T_0) \sin 2\omega t] \right\} I_0 \sin \omega t. \\ \therefore \frac{V(t)}{I_0} &\approx R_0(T_0) \sin \omega t + \frac{dR(T_0)}{dT} \frac{\chi_0(T_0)P_0}{2} \sin \omega t \\ &\quad + \frac{dR_0(T_0)}{dT} \frac{P_0}{4} [\chi'(2\omega, T_0) \sin \omega t - \chi''(2\omega, T_0) \cos \omega t - \chi'(2\omega, T_0) \sin 3\omega t + \chi''(2\omega, T_0) \cos 3\omega t]. \end{aligned} \quad (6)$$

Thus, for an input of $I(t) = I_0 \sin \omega t$, the Fourier series of $V(t)/I_0$ has been analytically derived up to the 3ω components. Following previous studies [17–19], we introduce $Z^{n\omega}$ to describe the resulting in-phase and out-of-phase electrical responses of the $n\omega$ components ($n = 1, 3$); i.e., $\text{Re } Z^{n\omega} \equiv \text{Re } \mathcal{V}^{n\omega}(\omega, I_0)/I_0$ and $\text{Im } Z^{n\omega} \equiv \text{Im } \mathcal{V}^{n\omega}(\omega, I_0)/I_0$, where $\mathcal{V}^{n\omega}(\omega, I_0)$ is the $n\omega$ Fourier component of $V(t)$ under an AC current with ω . The real and imaginary

parts of $Z^{n\omega}$ are given by:

$$\text{Re } Z^{1\omega}(\omega, I_0, T_0) - R_0(T_0) = \frac{dR_0(T_0)}{dT} \frac{P_0(I_0)}{4} [2\chi_0(T_0) + \chi'(2\omega, T_0)], \quad (7)$$

$$\text{Im } Z^{1\omega}(\omega, I_0, T_0) = -\frac{dR_0(T_0)}{dT} \frac{P_0(I_0)}{4} \chi''(2\omega, T_0), \quad (8)$$

$$\text{Re } Z^{3\omega}(\omega, I_0, T_0) = -\frac{dR_0(T_0)}{dT} \frac{P_0(I_0)}{4} \chi'(2\omega, T_0), \quad (9)$$

$$\text{Im } Z^{3\omega}(\omega, I_0, T_0) = \frac{dR_0(T_0)}{dT} \frac{P_0(I_0)}{4} \chi''(2\omega, T_0). \quad (10)$$

Note that the right-hand sides of Eqs. (7)–(10) are I_0 dependent via $P_0 = R_{2\text{probe}} I_0^2$, and thus, they represent nonlinear responses. The emergence of these nonlinear terms can be qualitatively understood as follows: Under an AC current with angular frequency ω , the sample temperature and resistance are time-varying, with a 2ω modulation; the 2ω resistance modulation couples with the AC current with ω , giving rise to additional output voltage modulations of both ω and 3ω . Thus, $\text{Im } Z^{1\omega}(\omega, I_0)$ and $\text{Im } Z^{3\omega}(\omega, I_0)$ appear due to a delay of the thermal response (i.e., χ'').

Note that regarding the nonlinear parts of the Joule-heating-induced AC electrical response, the following relations hold at low frequencies, $\omega \ll \omega_c = 1/(2\tau_{\text{therm}})$:

$$\left| \frac{\text{Im } Z^{1\omega}}{\text{Re } Z^{1\omega} - R_0} \right| = \frac{\chi''(2\omega, T_0)}{2\chi_0(T_0) + \chi'(2\omega, T_0)} \ll 1 \quad \text{for } \omega \ll \omega_c. \quad (11)$$

$$\left| \frac{\text{Im } Z^{3\omega}}{\text{Re } Z^{3\omega}} \right| = \frac{\chi''(2\omega, T_0)}{\chi'(2\omega, T_0)} \ll 1 \quad \text{for } \omega \ll \omega_c. \quad (12)$$

These equations indicate that at low ω , the nonlinearity is observed mainly in the real part, rather than in the imaginary part. These characteristics are also evident in the Cole-Cole representation [Figs. 4(a) and (b)], in which $\text{Re } Z^{1\omega} - R_0$ is adopted for the real axis for clarity. In the Cole-Cole representation of $Z^{3\omega}$, the ω -evolving trajectory starts somewhere on the real axis at DC and converges to the origin at high ω [Fig. 4(b)]. This behavior indicates that the Joule-heating-induced AC electrical response has dissipative characteristics. Contrastingly, when nonlinear $Z^{1\omega}$ and $Z^{3\omega}$ are caused by the nonlinear inductance, the nonlinear change should exclusively appear in the imaginary part; that is, $|\text{Im } Z^{1\omega}| \gg |\text{Re } Z^{1\omega} - R_0|$ and $|\text{Im } Z^{3\omega}| \gg |\text{Re } Z^{3\omega}|$ should hold at low ω . In the Cole-Cole representation, these nondissipative characteristics are observed as shown in Figs. 4(c) and (d). In particular, the ω -evolving trajectory of $Z^{3\omega}$ should start from the origin at DC [Fig. 4(d)], which is distinctly different from the $Z^{3\omega}$ caused by Joule heating [Fig. 4(b)]. Thus, the Cole-Cole represen-

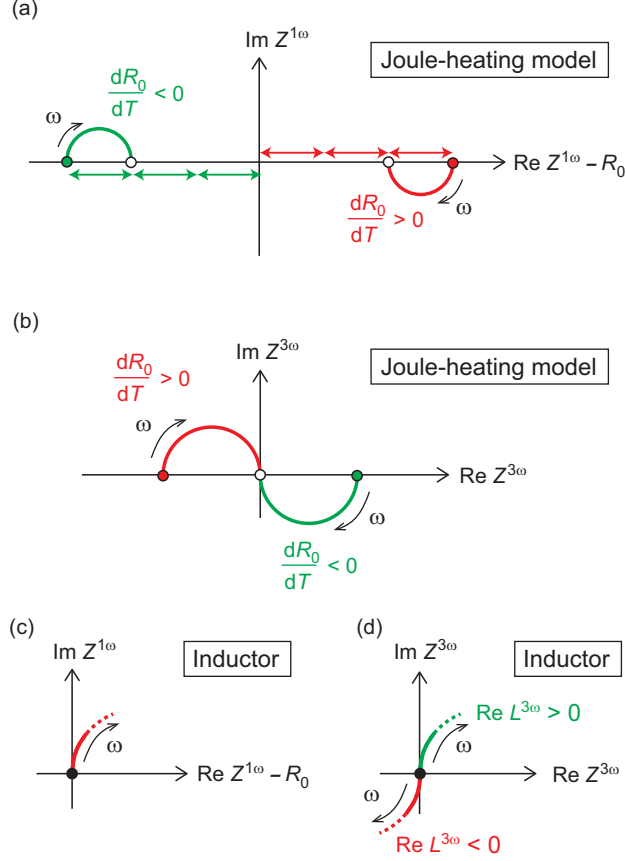


FIG. 4. Schematic Cole-Cole representation of the AC electrical response. (a, b) Cole-Cole representations of $Z^{1\omega}$ (a) and $Z^{3\omega}$ (b) under Joule heating. R_0 represents the DC linear response impedance. Schematics are drawn for both the cases of $dR_0/dT > 0$ and $dR_0/dT < 0$. (c, d) Cole-Cole representations of $Z^{1\omega}$ (c) and $Z^{3\omega}$ (d) of a nonlinear inductor element.

tation provides key insight into whether the observed nonlinear AC electrical response has dissipative or nondissipative characteristics.

C. Answers to questions I–III

Below, we show that the Joule-heating-induced AC electrical response expressed by Eqs. (7)–(10) satisfies all the types of behavior highlighted in questions I–III. We begin by answering question III. Below we use T to denote the sample-holder temperature, which corresponds to T_0 of the previous section.

Answer to question III. As indicated by Eqs. (8)–(10), the temperature dependences of $\text{Im } Z^{1\omega}$ ($= -\text{Im } Z^{3\omega}$) and $\text{Re } Z^{3\omega}$ involve that of $P_0(T) \times dR_0/dT$. Thus, the $\text{Im } Z^{1\omega/3\omega} - T$

profile is correlated with dR_0/dT . Since $P_0(T) = (R_0(T) + R_{\text{contact}}(T))I_0^2$, whether dR_0/dT or $R_0 \times dR_0/dT$ better describes the $\text{Im } Z^{1\omega/3\omega}-T$ profile depends on whether the Joule heating is dominant in the bulk or at the contacts of the current electrodes. If the Joule heat is produced exclusively in the bulk [i.e., $P_0(T) \approx R_0(T)I_0^2$], then $\text{Im } Z^{1\omega/3\omega}(T)$ would scale with $R_0 \times dR_0/dT$. If the Joule heat is mainly generated at the contacts of the current electrodes [i.e., $P_0(T) \approx R_{\text{contact}}(T)I_0^2$] and if $R_{\text{contact}}(T)$ only weakly depends on temperature, then $\text{Im } Z^{1\omega/3\omega}(T)$ would scale with dR_0/dT . This consideration accounts for the fact that $\text{Im } \rho^{1\omega}(T)$ scales well with either $-d\rho_0/dT$ or $-\rho_0 \times d\rho_0/dT$ depending on the report [Figs. 1(b), (d) and (f)]. However, note that the agreement should only be qualitative because this $\chi^*(T)$, which scales with the heat conductance and inversely scales with the heat capacitance, is also temperature dependent. At a very low temperature, the temperature increase for a given Joule heat can be pronounced, and thus, the scaling between the $\text{Im } Z^{1\omega/3\omega}-T$ and $d\rho_0/dT-T$ profiles may be worse. This circumstance may be related to the behavior below 10 K of $\text{Gd}_3\text{Ru}_4\text{Al}_{12}$ [Fig. 1(b)].

Answer to question II. The cutoff frequency ω_c of the Joule-heating-induced AC electrical response is determined by the thermal relaxation time of the sample: $\omega_c \approx 1/(2\tau_{\text{therm}})$. The thermal relaxation time depends on the system details, such as the sample dimensions and thermal contacts. For a millimeter-sized bulk sample, the typical value of τ_{therm} can be as long as $\sim 10^{-1}-10^{-2}$ s [25], which leads to $\sim 10^0-10^1$ Hz for the cutoff frequency of $\chi^*(\omega)$. For an exfoliated thin plate with a submicrometer thickness, the typical thermal relaxation time is $\sim 10^{-6}-10^{-3}$ s (depending on the thermal conductivity of the substrate) [26], which leads to $\sim 10^2-10^5$ Hz for the cutoff frequency. As shown below, the microfabricated CuIr_2S_4 and bulk MoTe_2 exhibit cutoff frequencies of 20 kHz and 1 Hz, respectively. Thus, in general, the cutoff frequency of the Joule-heating-induced AC electrical response can be much lower than the resonance frequency of the magnetic texture under consideration.

Answer to question I. For the Joule-heating-induced AC electrical response, an order of magnitude estimate of $\text{Im } \Delta\rho^{1\omega}(j_0)$ can be obtained by referring to $\text{Re } \Delta\rho^{1\omega}(j_0)$ and ω_c as follows:

$$\frac{\text{Im } \Delta\rho^{1\omega}(\omega, j_0, T)}{\text{Re } \Delta\rho^{1\omega}(\omega, j_0, T)} = \frac{\chi''(2\omega, T)}{2\chi_0(T) + \chi'(2\omega, T)}. \quad (13)$$

Note that the ratio of $\text{Im } \Delta\rho^{1\omega}(\omega, j_0, T)$ to $\text{Re } \Delta\rho^{1\omega}(\omega, j_0, T)$ does not depend on j_0 . Using

TABLE I. Order of magnitude estimate of $\text{Im } \Delta\rho^{1\omega}(\omega, j_0, T)/\omega$ for $\text{Gd}_3\text{Ru}_4\text{Al}_{12}$ [17], YMn_6Sn_6 [18], and FeSn_2 [19]. The parameters used for the calculations are taken from the literature [17–19] or Fig. 2.

Material	$\text{Gd}_3\text{Ru}_4\text{Al}_{12}$	YMn_6Sn_6	FeSn_2
Specimen	Microfabricated	Microfabricated	Bulk
Sample-holder temperature, T_0 [K]	15	270	350
Applied current density, j_0 [10^8 A m $^{-2}$]	4.0	2.5	0.8
Sample volume [μm^3]	13	290	8.9×10^4
Observed cutoff frequency, $\omega_c/2\pi$ [kHz]	20	1	0.1
Re $\Delta\rho^{1\omega}(j_0, T)$ at low ω [$\mu\Omega$ cm]	0.7	1.5	2.9
Im $\Delta\rho^{1\omega}(\omega, j_0, T)/\omega$ at low ω ($\ll \omega_c$) [$\mu\Omega$ cm s]	(<i>Cal.</i>)	-2×10^{-6}	-0.8×10^{-4}
	(<i>Exp.</i>)	-1.1×10^{-6}	-2.6×10^{-4}

Eq. (3) with $\alpha = 0$ for simplicity, we obtain:

$$\frac{\text{Im } \Delta\rho^{1\omega}(\omega, j_0, T)}{\omega} \approx -\frac{1}{3} \frac{\text{Re } \Delta\rho^{1\omega}(j_0, T)}{\omega_c} \quad \text{for } \omega \ll \omega_c, \quad (14)$$

where $\text{Re } \Delta\rho^{1\omega}(j_0, T)$ represents the low-frequency limit value. By referring to the $\text{Re } \Delta\rho^{1\omega}(j_0, T)$ and ω_c reported for $\text{Gd}_3\text{Ru}_4\text{Al}_{12}$ [17], YMn_6Sn_6 [18], and FeSn_2 [19], we calculate the $\text{Im } \Delta\rho^{1\omega}(\omega, j_0, T)/\omega$ at low ω ($\ll \omega_c$) for each system. The results are summarized in Table I. The calculated values are in good agreement with the reported data for all three systems. This correspondence on the order of magnitude demonstrates that the origin of the nonlinear $\text{Im } \Delta\rho^{1\omega}(j_0)$ observed in the experiments [17–19] lies in the delay of the nonlinear $\text{Re } \Delta\rho^{1\omega}(j_0)$ with a cutoff frequency ω_c . Another question that naturally arises here is what is the origin of the nonlinear $\text{Re } \Delta\rho^{1\omega}(j_0)$? The fact that the $\text{Im } \rho^{1\omega}(j_0)$ - T profiles scale well with the $(-d\rho_0/dT)$ - T or $(-\rho_0 \times d\rho_0/dT)$ - T profiles (Fig. 1) indicates that the nonlinear $\text{Re } \Delta\rho^{1\omega}(j_0)$ is also related to $d\rho_0/dT$. The simplest interpretation of this observation is that the nonlinear $\text{Re } \Delta\rho^{1\omega}(j_0)$ is caused by Joule heating. Thus, the similarity between the $\text{Im } \Delta\rho^{1\omega}$ - T and $(-d\rho_0/dT)$ - T profiles implies that $\text{Im } \Delta\rho^{1\omega}$ includes a considerable contribution of the Joule-heating-induced AC electrical response.

Others. Although unrelated to questions I–III, $\text{Im } Z^{1\omega} = -\text{Im } Z^{3\omega}$ is also a characteristic consequence of the Joule heating model.

IV. EXPERIMENTS

To experimentally test the Joule heating model, we measured the nonlinear AC electrical response for two conducting systems: a microfabricated CuIr_2S_4 crystal (sample dimensions of $20 \times 4 \times 1 \mu\text{m}^3$) and a bulk $1T'$ - MoTe_2 crystal ($1.3 \times 0.7 \times 0.14 \text{ mm}^3$); images of the two samples are shown in Figs. 9(a) and (b) in the APPENDIX. These materials exhibit no magnetic order, and a current-induced spin dynamics contribution to the AC electrical response can therefore be ruled out. In both materials, we find a good agreement between the experimental and expected results for the Joule-heating-induced AC electrical response. For readability, only results for the microfabricated CuIr_2S_4 are shown in the main text. Results for the bulk MoTe_2 are shown in Figs. 10 and 11 in the APPENDIX.

CuIr_2S_4 shows a first-order metal-insulator transition at $T_c \approx 230 \text{ K}$ [27, 28]. This material is paramagnetic and metallic (i.e., $d\rho_0/dT > 0$) above T_c , whereas it is nonmagnetic and semiconducting (i.e., $d\rho_0/dT < 0$) below T_c . Figures 5(a), (b), (c), and (d) display the temperature dependences of $\text{Re } \rho^{1\omega}$, $\text{Im } \Delta\rho^{1\omega}$, $\text{Re } \rho^{3\omega}$, and $\text{Im } \rho^{3\omega}$ at $\omega/2\pi = 6 \text{ kHz}$, respectively, measured at various current densities. Here, we display $\text{Im } \Delta\rho^{1\omega} \equiv \text{Im } \rho^{1\omega}(j_0) - \text{Im } \rho^{1\omega}(5.0 \times 10^7 \text{ A m}^{-2})$ only for $\text{Im } \rho^{1\omega}$ to subtract the contribution of the nonnegligible linear-response background; for the raw data of $\text{Im } \rho^{1\omega}$, see Fig. 9(c) in the APPENDIX. In contrast, for $\rho^{3\omega}$, we find that the background signal is not significant, so we display the raw data.

In the $\text{Re } \rho^{1\omega}-T$ profile [Fig. 5(a)], the apparent transition temperature clearly decreases with increasing current, indicating that the sample temperature is elevated from the sample-holder temperature, T_{holder} , by Joule heating. In the insulating phase, the four-probe resistance is $30\text{--}80 \Omega$ within $225\text{--}160 \text{ K}$, whereas the contact resistance is $\approx 20 \Omega$. Thus, the Joule heat is thought to be generated mainly in the bulk, rather than at the contacts of the current electrodes.

Figures 5(b)–(f) show characteristic features consistent with the Joule heating model. First, in the insulating phase, $\text{Im } \Delta\rho^{1\omega}$, $\text{Re } \rho^{3\omega}$ and $\text{Im } \rho^{3\omega}$ nonlinearly emerge as the AC current increases [Figs. 5(b)–(d)]. The signs of these quantities are consistent with Eqs. (8)–(10) for the case of $d\rho_0/dT < 0$. Second, the $\text{Im } \Delta\rho^{1\omega}-T$ profile agrees well with the $(-\rho_0 \times d\rho_0/dT)-T$ profile [Fig. 5(e)], consistent with the results expected when Joule heating occurs mainly in the bulk.. Third, $\text{Im } \Delta\rho^{1\omega} = -\text{Im } \rho^{3\omega}$ is well satisfied [Fig. 5(f)].

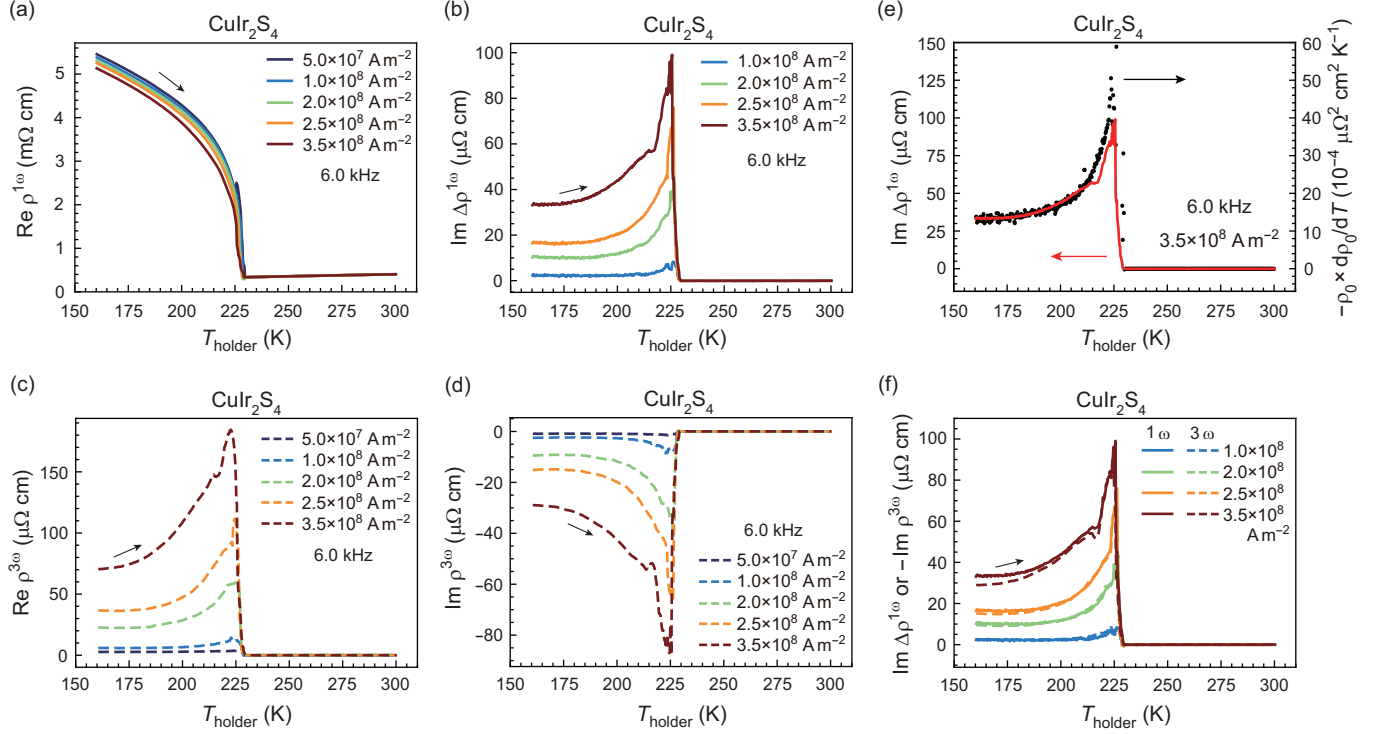


FIG. 5. Temperature dependence of the AC electrical response of CuIr_2S_4 measured at various current amplitudes. (a) $\text{Re } \rho^{1\omega}$, (b) $\text{Im } \Delta\rho^{1\omega}$, (c) $\text{Re } \rho^{3\omega}$, and (d) $\text{Im } \rho^{3\omega}$. The $\text{Im } \Delta\rho^{1\omega}$ shown in (b) is defined as $\text{Im } \Delta\rho^{1\omega} \equiv \text{Im } \rho^{1\omega}(j_0) - \text{Im } \rho^{1\omega}(5.0 \times 10^7 \text{ A m}^{-2})$. (e) Comparison between $\text{Im } \Delta\rho^{1\omega}$ and $-\rho_0 \times d\rho_0/dT$. The data were recorded in the heating process. (f) Comparison between $\text{Im } \Delta\rho^{1\omega}$ and $-\text{Im } \rho^{3\omega}$.

The frequency dependences and Cole-Cole representations of $\Delta\rho^{1\omega}$ and $\rho^{3\omega}$ at 210 K are shown in Figs. 6(a)–(f). Overall, the Cole-Cole representations [Figs. 6(c) and (f)] are consistent with the predictions of the Joule heating model for the case of $d\rho_0/dT < 0$ [Figs. 4(a) and (c)]. The lengths of the arc strings are approximately the same for both cases (200 $\mu\Omega$ cm). From the frequency dependence, the cutoff frequency in the present device is found to be ≈ 20 kHz. Note that this value is not an intrinsic quantity of the material but should depend on the sample volume, details of the thermal contacts, etc. In the bulk MoTe_2 , for instance, the cutoff frequency is as low as 1 Hz (see Fig. 11 in the APPENDIX), indicating that the sample dimensions are a crucial factor determining the cutoff frequency of the Joule-heating-induced AC electrical response. The cutoff frequency depends on temperature only weakly, except for at the transition point, at which it decreases to 7 kHz. This decrease in the cutoff frequency is ascribed to an apparent increase in the

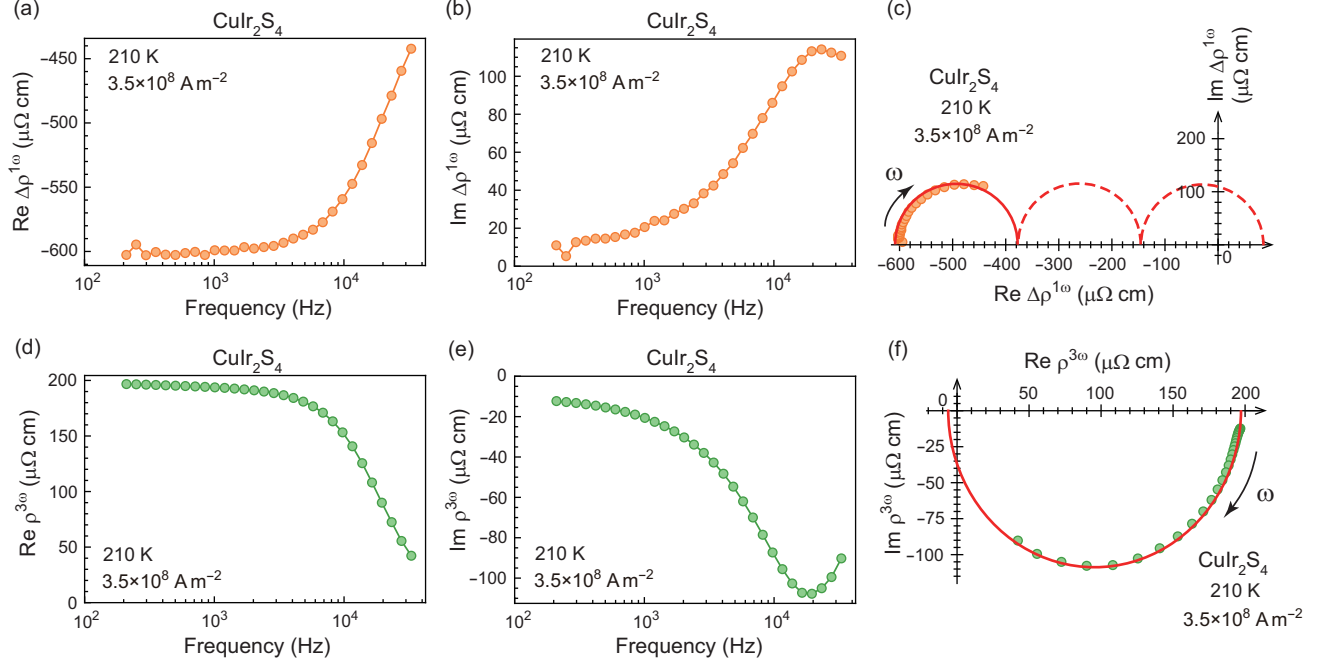


FIG. 6. Frequency dependence of the nonlinear AC electrical response of CuIr_2S_4 at 210 K. (a) $\text{Re } \Delta\rho^{1\omega}$, (b) $\text{Im } \Delta\rho^{1\omega}$, and (c) Cole-Cole representation of $\Delta\rho^{1\omega}$. $\Delta\rho^{1\omega}$ is defined as $\Delta\rho^{1\omega} \equiv \rho^{1\omega}(j_0) - \rho^{1\omega}(5.0 \times 10^7 \text{ A m}^{-2})$. (d) $\text{Re } \rho^{3\omega}$, (e) $\text{Im } \rho^{3\omega}$, and (f) Cole-Cole representation of $\rho^{3\omega}$. The data were recorded at $j_0 = 3.5 \times 10^8 \text{ A m}^{-2}$.

heat capacity at a first-order phase transition.

For an applied current density below $5 \times 10^8 \text{ A m}^{-2}$, the nonlinear AC electrical response is difficult to detect in the metallic phase above 230 K. To observe the sign of the nonlinear behavior in the metallic phase, we measured the j_0 - $\text{Im } \Delta\rho^{1\omega}$ profile up to a higher current density, and the results are shown in Fig. 7. The finite nonlinear $\text{Im } \Delta\rho^{1\omega}$ exhibits a detectable magnitude in the metallic phase when j_0 exceeds $7 \times 10^8 \text{ A m}^{-2}$, and its sign is negative. Thus, we confirm that the sign of the nonlinear $\text{Im } \Delta\rho^{1\omega}$ is negative in the metallic phase ($d\rho_0/dT > 0$), whereas it is positive in the insulating phase ($d\rho_0/dT < 0$). The relationship between the signs of $\text{Im } \Delta\rho^{1\omega}$ and $d\rho_0/dT$ is consistent with the Joule heating model.

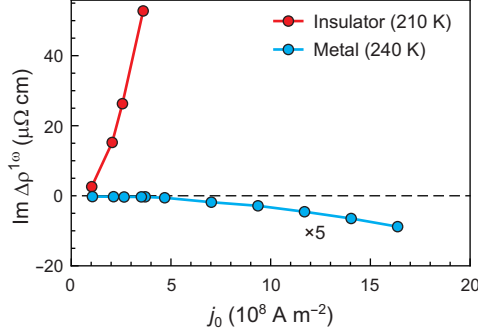


FIG. 7. Current-density dependence of $\text{Im } \Delta\rho$ in the insulating and metallic phases. $\Delta\rho^{1\omega}$ is defined as $\Delta\rho^{1\omega} \equiv \text{Im } \rho^{1\omega}(j_0) - \rho^{1\omega}(5.0 \times 10^7 \text{ A m}^{-2})$.

V. DISCUSSION

By measuring two different materials that exhibit no magnetic order, i.e., CuIr_2S_4 (in the main text) and MoTe_2 (in the APPENDIX), we have confirmed that the observed nonlinear AC electrical response is consistent with the Joule-heating-induced AC electrical response. Phenomenologically, the nonlinear $\Delta Z(j_0)$ is likely described by the sum of dissipative and nondissipative mechanisms: $\Delta Z(j_0) = \Delta Z_{\text{diss}}(j_0) + \Delta Z_{\text{nondiss}}(j_0)$, where ΔZ_{diss} and $\Delta Z_{\text{nondiss}}$ represent the nonlinear impedances due to dissipative and nondissipative mechanisms, respectively. Note that by definition, at low ω , $\text{Re } \Delta Z_{\text{diss}} \gg \text{Im } \Delta Z_{\text{diss}}$, and $\text{Re } \Delta Z_{\text{nondiss}} \ll \text{Im } \Delta Z_{\text{nondiss}}$. The inductor mechanism due to the EEF caused by a pinned magnetic texture belongs to $\Delta Z_{\text{nondiss}}$, whereas the Joule-heating-induced AC electrical response belongs to ΔZ_{diss} . Since we found $\text{Re } \Delta\rho \gg \text{Im } \Delta\rho$ at low ω in previous studies [17–19], we focused on ΔZ_{diss} and considered $\Delta Z_{\text{Joule}}(j_0)$ to be a plausible candidate. We have thus found that regarding $\Delta Z(j_0)$, both the temperature dependence and magnitude are similar to those expected for $\Delta Z_{\text{Joule}}(j_0)$, regardless of whether the material under consideration exhibits a magnetic order (as in [17–19]) or not (as in this study). This finding implies that $\Delta Z_{\text{Joule}}(j_0)$ is presumably the most prominent among several coexisting nonlinear mechanisms, and therefore, the observed $\Delta Z(j_0)$ cannot straightforwardly be attributed to any subdominant mechanism of the nonlinear electrical response, such as the spin-related $\Delta Z_{\text{nondiss}}$.

In general, a comparison of the real and imaginary parts of the AC electrical response at low frequencies would provide key insights into the fundamental properties of the nonlinear

AC impedance under consideration. In previous experiments, the fact that a nonlinear $\text{Im } \Delta\rho$ is accompanied by an even larger nonlinear $\text{Re } \Delta\rho$ was not deeply considered. To understand the nature of the nonlinear AC electrical response, the real and imaginary parts must be examined on an equal footing.

VI. CONCLUSION

Aiming to clarify fundamental questions that arose in the previous experiments on so-called emergent inductors, we have considered the impact of time-varying Joule heating on the AC electrical responses. From a theoretical point of view, several key characteristics of the Joule-heating-induced AC electrical response are clarified, and they provide natural explanations for the hitherto unexplained behavior observed in emergent-inductor experiments. To further examine the Joule-heating-induced AC electrical response, we have performed experiments on two materials that exhibit no magnetic order, i.e., CuIr_2S_4 and $1\text{T}'\text{-MoTe}_2$, and confirmed the characteristics of the Joule heating model. In particular, in our microfabricated CuIr_2S_4 , a cutoff frequency of ≈ 20 kHz is observed, which is in agreement with the value reported for the microfabricated noncollinear magnet $\text{Gd}_3\text{Ru}_4\text{Al}_{12}$.

The Joule-heating-induced AC electrical response inevitably gives rise to either a positive $\text{Im } Z$ (when $d\rho_0/dT < 0$) or a negative $\text{Im } Z$ (when $d\rho_0/dT > 0$), unless the Joule heating is negligible and the measurement frequency is far greater than the inverse of the thermal response time. Even temperature oscillations as small as 0.1 K cause a $\text{Im } \Delta\rho$ of considerable magnitude, which is much larger than that expected based on the linear-response EEF. In previous experiments on emergent inductors, the nonlinear $\text{Im } \rho$ below the cutoff frequency was discussed, and the nonlinearity more pronouncedly occurred in $\text{Re } \rho$ than in $\text{Im } \rho$. Our results thus suggest that the reported data regarding emergent inductors need to be reconsidered by taking the impact of the Joule heating into account.

Acknowledgments

F.K., S.F. and W.K. thank T. Yokouchi and A. Kitaori for providing us with the raw data from the literature [17, 18]. F.K., S.F. and W.K. thank T. Yokouchi and S. Maekawa for fruitful discussions. We thank Y. Tokumura for the synthesis of CuIr_2S_4 . This work was

partially supported by JSPS KAKENHI (Grants No. 21H04442 and No. 23K03291), JST CREST (Grants No. JPMJCR1874 and No. JPMJCR20T1).

APPENDIX

1. Magnetic field dependence of $d\rho/dT$ in $\text{Gd}_3\text{Ru}_4\text{Al}_{12}$ at 5 K

Figure 8(a) shows the magnetic-field dependence of $\text{Re } \rho^{1\omega}$ in $\text{Gd}_3\text{Ru}_4\text{Al}_{12}$ at $T_{\text{holder}} = 5.1$ and 5.3 K, which was measured at a current density in the nonlinear regime, $j_0 = 3.3 \times 10^8 \text{ A m}^{-2}$. Although these data are not in the linear-response regime, we estimate the $d\rho_0/dT-H$ profile by simply taking the difference between the two sets of data divided by the small T increment, 0.2 K. The results are shown in Fig. 8(b). Figure 8(c) shows the $\text{Im } \rho^{1\omega}-H$ profile at $T_{\text{holder}} = 5.1$ K under the same current density. Note that the data are not $\text{Im } \Delta\rho^{1\omega}$, so they should include the linear-response background signal. For instance, in Fig. 2, $\text{Im } \rho^{1\omega}$ shows a T -dependent negative signal even in the linear-response regime. This signal may vary with the magnetic field. Given this uncertainty, the $d\rho/dT-H$ profile exhibits a complicated sharp structure, which is similar to that seen in Fig. 8(c). This similarity, at least on a qualitative level, leads us to conclude that there is a considerable correlation between $d\rho_0/dT$ and $\text{Im } \rho$.

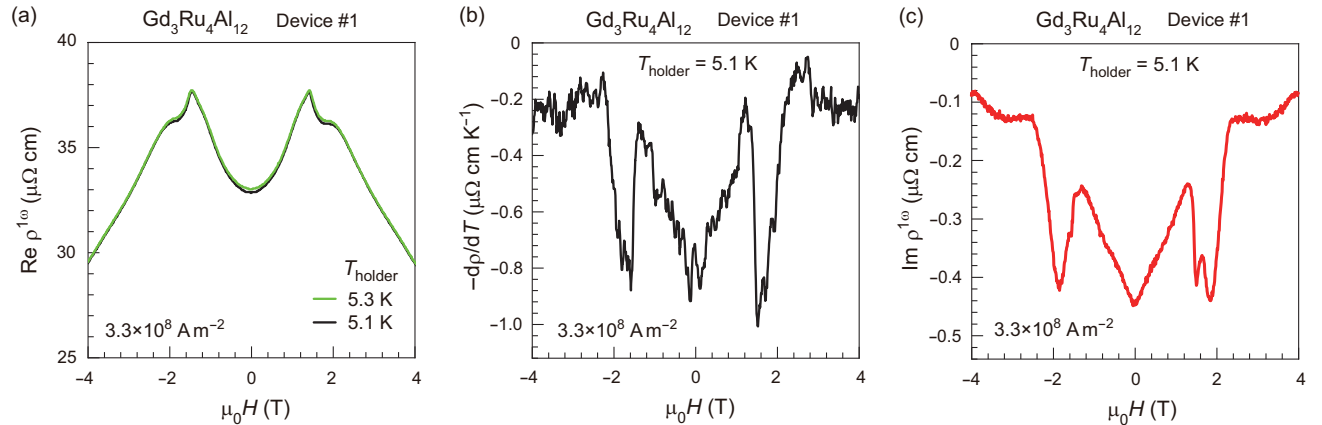


FIG. 8. (a) Magnetic-field dependence of $\text{Re } \rho^{1\omega}$ in $\text{Gd}_3\text{Ru}_4\text{Al}_{12}$ at $T_{\text{holder}} = 5.1$ and 5.3 K, measured at a relatively high current density, $j_0 = 3.3 \times 10^8 \text{ A m}^{-2}$. (b) Estimated $(-d\rho_0/dT)-H$ profile under $j_0 = 3.3 \times 10^8 \text{ A m}^{-2}$. (c) $\text{Im } \rho^{1\omega}-H$ profile under $j_0 = 3.3 \times 10^8 \text{ A m}^{-2}$. The data were collected from the raw data published in the literature [17].

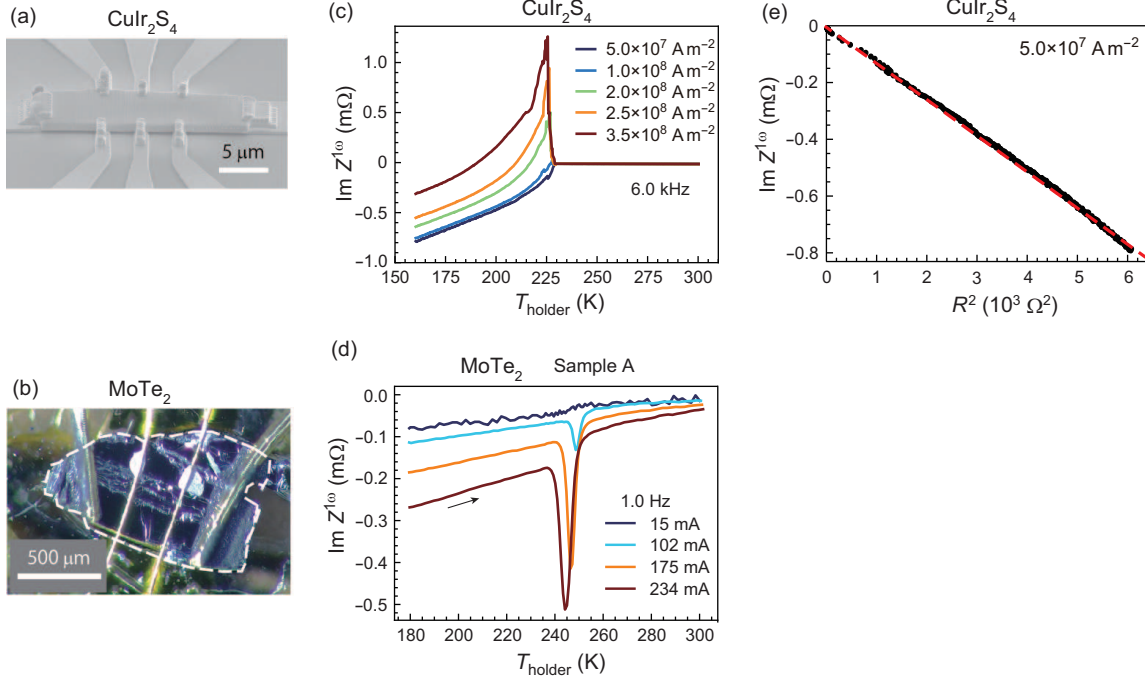


FIG. 9. (a) Scanning electron microscopy image of the microfabricated CuIr_2S_4 device used in this study. (b) Photograph of the bulk MoTe_2 used in this study. (c) Raw data of the $\text{Im } \rho^{1\omega}-T$ profile of the microfabricated CuIr_2S_4 . (d) Raw data of the $\text{Im } Z^{1\omega}-T$ profile of the microfabricated MoTe_2 . (e) R^2 vs $\text{Im } Z^{1\omega}$ plot for the impedance under a weak AC current of $5.0 \times 10^7 \text{ A m}^{-2}$.

2. Methods

The images of the microfabricated CuIr_2S_4 device and the bulk MoTe_2 are shown in Figs. 9(a) and (b), respectively. In the experiments on MoTe_2 , we used carbon paste for the current electrodes to facilitate the Joule heating; the resistivity of MoTe_2 is too low to achieve a Joule heating in bulk with use of $\sim 100 \text{ mA}$ for the case of bulk crystal.

Figures 9(c) and (d) show the raw data of the $\text{Im } \rho^{1\omega}-T$ profile of the microfabricated CuIr_2S_4 device and $\text{Im } Z^{1\omega}-T$ profile of the bulk MoTe_2 crystal, respectively. The linear-response background signal is nonmonotonically T dependent in the microfabricated CuIr_2S_4 device, whereas it is relatively small and weakly T dependent in the bulk MoTe_2 crystal. The linear-response background in the CuIr_2S_4 device is likely due to the impact of the stray capacitance C , which gives rise to a linear-response background of $-i\omega R_0^2 C$ [15], where R_0 is the linear-response resistance. $\text{Im } Z^{1\omega}$ is proportional to R_0^2 in the present temperature range [Fig. 9(e)], indicating that the $(-R_0^2 C)$ -type background dominates the imaginary part

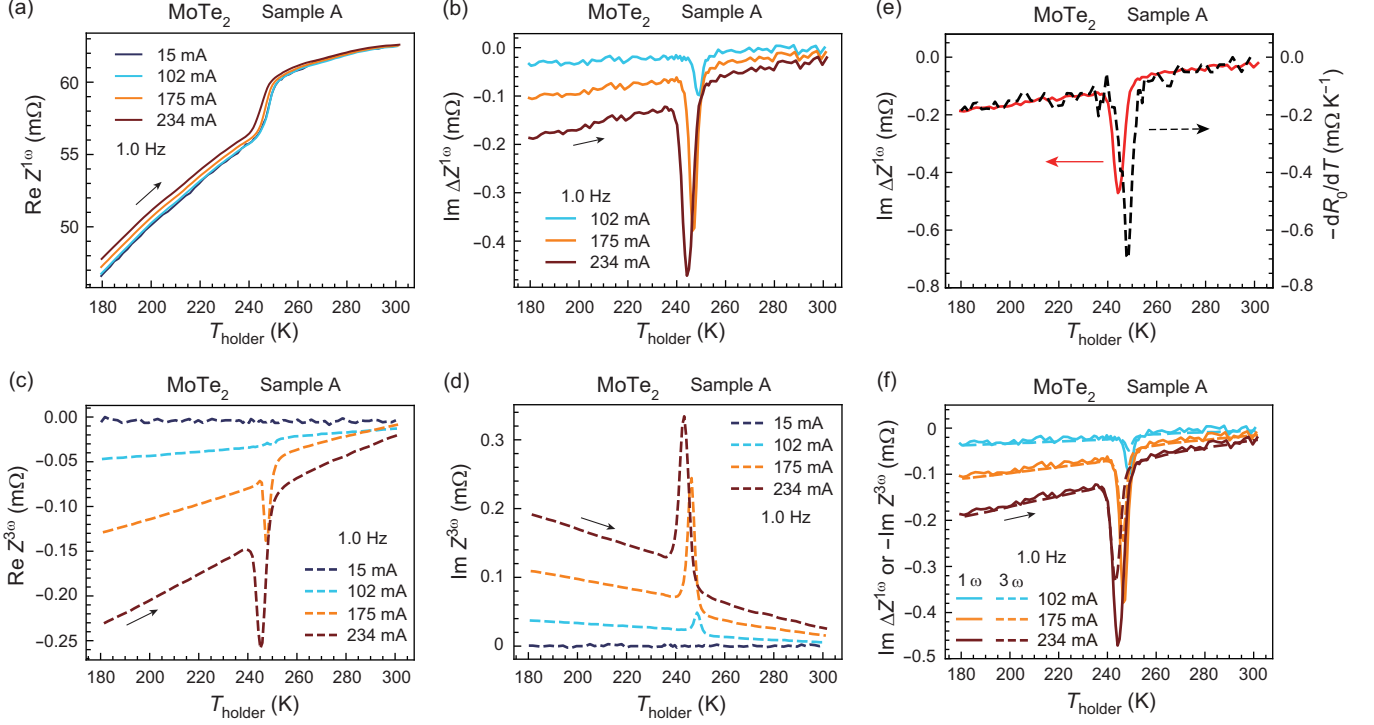


FIG. 10. Temperature dependence of AC electrical response of MoTe₂ measured at various current amplitudes. (a) $\text{Re } Z^{1\omega}$, (b) $\text{Im } Z^{1\omega}$, (c) $\text{Re } Z^{3\omega}$, and (d) $\text{Im } Z^{3\omega}$. The data were recorded in the heating process. (e) Comparison between $\text{Im } \Delta Z^{1\omega}$ and $-dR_0/dT$. (f) Comparison between $\text{Im } \Delta Z^{1\omega}$ and $-\text{Im } Z^{3\omega}$.

of the linear-response signal of the microfabricated sample. Since the nonlinearly enhanced electrical response is the main focus of this study, we present $\Delta \text{Im } Z^{1\omega}$, which represents a nonlinear change from the linear-response value.

3. Nonlinear AC electrical response of MoTe₂ bulk crystal

MoTe₂ shows a clear change in dR_0/dT through a first-order structural phase transition at $T_c \approx 250$ K [29], and thus, this feature is helpful to study the correlation between $\text{Im } Z^{1\omega}$ and $-dR_0/dT$.

Figures 10(a), (b), (c), and (d) display the temperature dependences of $\text{Re } Z^{1\omega}$, $\text{Im } \Delta Z^{1\omega}$, $\text{Re } Z^{3\omega}$, and $\text{Im } Z^{3\omega}$ at $\omega/2\pi = 1$ Hz, respectively, measured using various current amplitudes. In the $\text{Re } Z^{1\omega}-T$ profile [Fig. 10(a)], the apparent transition temperature clearly decreases as the current increases, indicating that the sample temperature is increased from

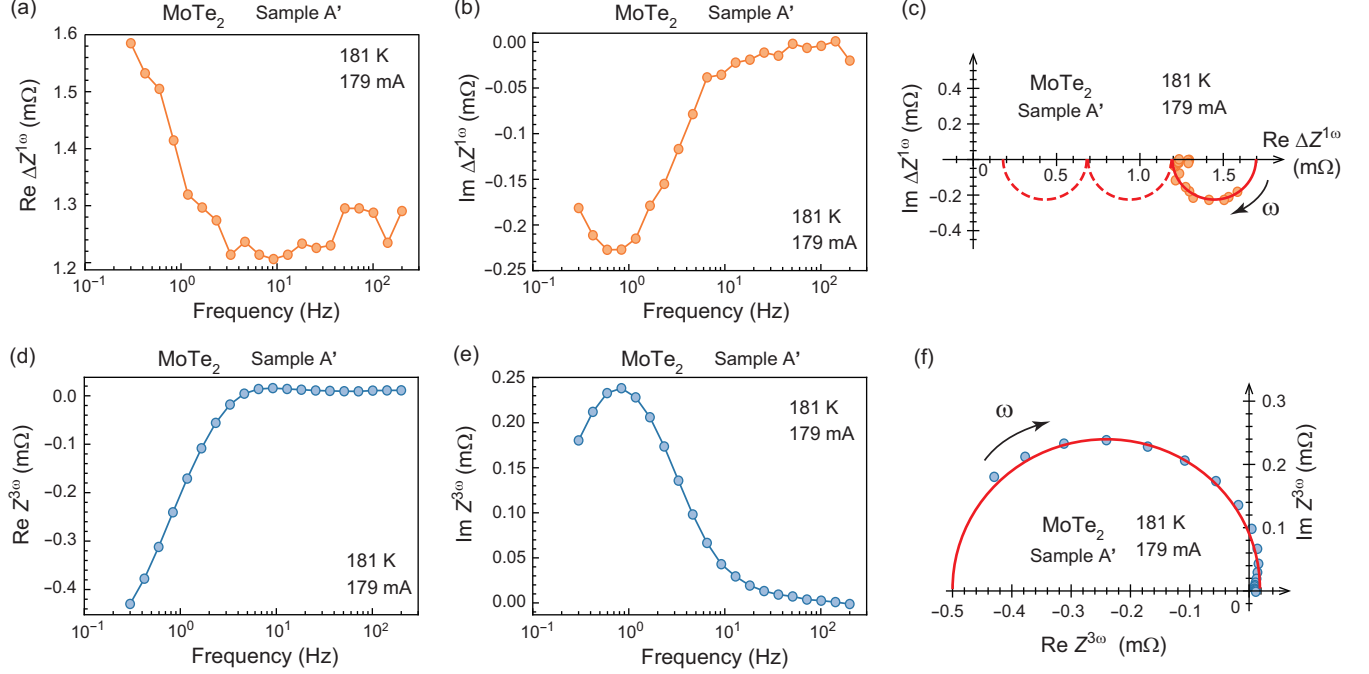


FIG. 11. Frequency dependence of the nonlinear AC electrical response of MoTe₂ at 181 K. (a) $\text{Re } \Delta Z^{1\omega}$, (b) $\text{Im } \Delta Z^{1\omega}$, and (c) Cole-Cole representation of $\Delta Z^{1\omega}$. (d) $\text{Re } Z^{3\omega}$, (e) $\text{Im } Z^{3\omega}$, and (f) Cole-Cole representation of $Z^{3\omega}$. The data were recorded using an AC current of $j_0 = 179$ mA. As the experiments progressed, the contact resistance changed from the state shown in Fig. 10, and the sample is therefore labelled Sample A', instead of A. The geometries of Sample A and Sample A' are exactly the same.

the sample-holder temperature, T_{holder} , by Joule heating. In Figs. 10(b)–(f), characteristic features consistent with the Joule heating model can be observed. First, $\text{Im } \Delta Z^{1\omega}$, $\text{Re } Z^{3\omega}$ and $\text{Im } Z^{3\omega}$ nonlinearly emerge as the AC current increases [Figs. 10(b)–(d)]. Second, the $\text{Im } \Delta Z^{1\omega}$ – T profile qualitatively agrees well with the $(-dR_0/dT)$ – T profile [Fig. 10(e)], consistent with the results expected when Joule heating occurs mainly at the contacts. Third, the relation of $\text{Im } \Delta Z^{1\omega} = -\text{Im } Z^{3\omega}$ is well satisfied except for in the transition region at 245 K [Fig. 10(f)]. The breakdown of $\text{Im } \Delta Z^{1\omega} = -\text{Im } Z^{3\omega}$ at 245 K may be reasonable considering that Eq. (2) is generally not applicable at a first-order phase transition because of the latent heat.

The frequency dependences and Cole-Cole representations of $\Delta Z^{1\omega}$ and $Z^{3\omega}$ at 180 K are shown in Figs. 11(a)–(f). They are also consistent with the predictions of the Joule heating model for the case of $dR_0/dT > 0$, although $Z^{1\omega}$ appears to be more susceptible to the

linear-response background than $Z^{3\omega}$. In the Cole-Cole representations of $Z^{1\omega}$ and $Z^{3\omega}$, the lengths of the arc strings are approximately the same (0.5 m Ω). The cutoff frequency of the nonlinear AC electrical response is estimated as ≈ 1 Hz. This frequency is typical for the thermal response in a bulk crystal, as often reported in AC-temperature calorimetry experiments [30].

* kagawa@phys.titech.ac.jp

References

- [1] J. C. Slonczewski, *J. Magn. Magn. Mater.* **159**, L1 (1996).
- [2] L. Berger, *Phys. Rev. B* **54**, 9353 (1996).
- [3] N. Nagaosa, *Jpn. J. Appl. Phys.* **58**, 120909 (2019).
- [4] G. E. Volovik, *J. Phys. C* **20**, L83 (1987).
- [5] S. E. Barnes and S. Maekawa, *Phys. Rev. Lett.* **98**, 246601 (2007).
- [6] T. Nattermann, Y. Shapir and I. Vilfan, *Phys. Rev. B* **42**, 8577 (1990).
- [7] P. Chauve, T. Giamarchi and P. L. Doussal, *Phys. Rev. B* **62**, 6241 (2000).
- [8] W. Kleemann, *Annu. Rev. Mater. Res.* **37**, 415 (2007).
- [9] G. Tatara and H. Kohno, *Phys. Rev. Lett.* **92**, 086601 (2004).
- [10] A. Thiaville, Y. Nakatani, J. Miltat and Y. Suzuki, *Europhys. Lett.* **69**, 990 (2005).
- [11] G. Tatara, T. Takayama, H. Kohno, J. Shibata, Y. Nakatani, and H. Fukuyama, *J. Phys. Soc. Jpn.* **75**, 064708 (2006).
- [12] T. Koyama, D. Chiba, K. Ueda, K. Kondou, H. Tanigawa, S. Fukami, T. Suzuki, N. Ohshima, N. Ishiwata, Y. Nakatani, K. Kobayashi and T. Ono, *Nat. Mat.* **10**, 194 (2011).
- [13] G. Tatara, H. Kohno and J. Shibata, *Phys. Rep.* **468**, 213 (2008).
- [14] C. Burrowes, A. P. Mihai, D. Ravelosona, J.-V. Kim, C. Chappert, L. Vila, A. Marty, Y. Samson, F. Garcia-Sanchez, L. D. Buda-Prejbeanu, I. Tudosa, E. E. Fullerton and J.-P. Attané, *Nat. Phys.* **6**, 17 (2010).
- [15] S. Furuta, S. H. Moody, K. Kado, W. Koshibae and F. Kagawa. *npj Spintronics* **1**, 1 (2023).
- [16] J. D. Jackson, *Classical Electrodynamics, 3rd Edition.* (Wiley, 1998).

- [17] T. Yokouchi, F. Kagawa, M. Hirschberger, Y. Otani, N. Nagaosa and Y. Tokura, *Nature* **586**, 232 (2020).
- [18] A. Kitaori, N. Kanazawa, T. Yokouchi, F. Kagawa, N. Nagaosa and Y. Tokura, *Proc. Natl. Acad. Sci. U.S.A.* **118**, e2105422118 (2021).
- [19] T. Yokouchi, Y. Yamane, Y. Araki, J. Ieda and Y. Shiomi, arXiv:2312.01553.
- [20] A. Kitaori, J. S. White, N. Kanazawa, V. Ukleev, D. Singh, Y. Furukawa, T. Arima, N. Nagaosa and Y. Tokura, *Phys. Rev. B* **107**, 024406 (2023).
- [21] M. P. Shaw, V. V. Mitin, E. Schöll, E. and H. L. Grubin, *The Physics of Instabilities in Solid State Electron Devices. Plenum Press* (New York), 1992.
- [22] See Supplemental Material at <http://XXXXXX> for the supplemental note for a hypothetical negative coefficient of dI/dT .
- [23] E. Saitoh, H. Miyajima, T. Yamaoka and G. Tatara, *Nature* **432**, 203 (2004).
- [24] D. Perconte, S. Mañas-Valero, E. Coronado, I. Guillamón, and H. Suderow, *Phys. Rev. Appl.* **13**, 054040 (2020).
- [25] H. Oike, A. Kikkawa, N. Kanazawa, Y. Taguchi, M. Kawasaki, Y. Tokura and F. Kagawa, *Nat. Phys.* **12**, 62 (2016).
- [26] H. Oike, M. Kamitani, Y. Tokura and F. Kagawa, *Sci. Adv.* **4**, eaau3489 (2018).
- [27] T. Furubayashi, T. Matsumoto, T. Hagino and S. Nagata, *J. Phys. Soc. Jpn.* **63**, 3333 (1994).
- [28] P. G. Radaelli, Y. Horibe, M. J. Gutmann, H. Ishibashi, C. H. Chen, R. M. Ibberson, Y. Koyama, Y.-S. Hor, V. Kiryukhin and S.-W. Cheong, *Nature* **416**, 155 (2002).
- [29] K. Zhang, C. Bao, Q. Gu, X. Ren, H. Zhang, K. Deng, Y. Wu, Y. Li, J. Feng, and S. Zhou, *Nat. Commun.* **7**, 135552 (2016).
- [30] P. F. Sullivan and G. Seidel, *Phys. Rev.* **173**, 679 (1968).

SUPPLEMENTAL MATERIAL

In Supplemental Material, we show that the negative nonlinear reactance reported in previous experimental studies [17–19] is not a manifestation of negative nonlinear inductance. In previous experimental reports, the impedance at the fundamental and higher harmonic frequencies was measured for the input frequency $\omega/(2\pi)$ using the lock-in technique. The typical experimental setup is displayed in Fig. S1: a magnetic material, a load resistor with resistance, R_L , and an AC voltage output of the lock-in amplifier, $V_0 \sin \omega t$, are connected in series. For simplicity, we consider a sample with a two-probe configuration and do not explicitly consider the contact resistance. The current flowing through the circuit, $\mathcal{I}^{1\omega}(\omega)$ [the 1ω Fourier component of $I(t)$], was determined from the voltage drop at the load resistor, and the voltage drop at the sample, $\mathcal{V}_s^{1\omega}(\omega)$ [the 1ω Fourier component of $V_s(t)$], was measured. Then, they defined the complex impedance $Z^{1\omega}(\omega, \mathcal{I})$ at $\mathcal{I}^{1\omega}(\omega)$ by $\mathcal{V}_s^{1\omega}(\omega)/\mathcal{I}^{1\omega}(\omega)$. Note that this definition was also used for a large $\mathcal{I}^{1\omega}(\omega)$ such that the proportionality between $\mathcal{V}_s^{1\omega}(\omega)$ and $\mathcal{I}^{1\omega}(\omega)$ is no longer valid. From a theoretical perspective, they defined an emergent inductor as an element showing the following voltage drop:

$$V_s(t) = R_s I(t) + L_0 \left(1 + AI(t)^2 + BI(t)^4 + \dots \right) \frac{dI}{dt}, \quad (\text{S1})$$

where R_s is the resistance of the sample, L_0 denotes the inductance in the linear response, and A and B are coefficients representing the nonlinearity related to the inductive response. From an energetic perspective, Eq. (S1) corresponds to the fact that under current I , the inductive element with a finite resistance can store the following energy:

$$E_L(I(t)) = L_0 \left(\frac{1}{2} I(t)^2 + \frac{1}{4} AI(t)^4 + \frac{1}{6} BI(t)^6 + \dots \right). \quad (\text{S2})$$

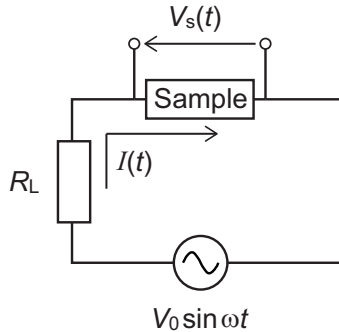


Fig. S 1. Typical experimental circuit used for measurement of the complex impedance.

Note that the inductive term in Eq. (S1), multiplied by I , is equal to dE_L/dt , indicating the relationship between the inductive electric response and the energy stored in the inductor. Given Eq. (S1), the circuit equation of the measurement system is given as:

$$\begin{aligned} V_0 \sin \omega t &= (R_L + R_s)I(t) + L_0 \left(1 + AI(t)^2 + BI(t)^4 + \dots \right) \frac{dI}{dt} \\ &= RI(t) + L_0 \left(1 + AI(t)^2 + BI(t)^4 + \dots \right) \frac{dI}{dt}, \end{aligned} \quad (\text{S3})$$

where V_0 is the output voltage amplitude of the lock-in amplifier and R is the sum of the sample and load resistances. Experimentally, they observed $\text{Im}[\mathcal{V}_s^{1\omega}(\omega)/\mathcal{I}^{1\omega}(\omega)] \approx -|\eta|\omega$ at low frequencies, especially when the flowing current is large under a large V_0 . This observation was interpreted as indicating that the coefficient of dI/dt in Eq. (S3) became negative under large currents. However, it has not been discussed whether Eq. (S3) truly shows $\text{Im}[\mathcal{V}_s^{1\omega}(\omega)/\mathcal{I}^{1\omega}(\omega)] \approx -|\eta|\omega$ when the coefficient of dI/dt is negative at a large I . Therefore, the correspondence between the experimental observations and Eqs. (S1)–(S3) remains unclear. In fact, as shown below, the solution of Eq. (S3) has instability towards self-sustained oscillations when the coefficient of dI/dt becomes negative at a large I , and it does not show an electric response such that $\text{Im}[\mathcal{V}_s^{1\omega}(\omega)/\mathcal{I}^{1\omega}(\omega)] \approx -|\eta|\omega$; i.e., the experimental observations are not described by Eqs. (S1)–(S3). In the following, we numerically examine the nature of the nonlinear negative inductance represented by Eqs. (S1)–(S3).

Equation (S3) is complicated because the coefficient of dI/dt is time dependent and may change the sign during the time evolution. To gain insights into Eq. (S3), it would be instructive to begin with a simpler case. We consider a different form of circuit equation, which is nonlinear with respect to the input voltage amplitude, V_0 , instead of the current:

$$\begin{aligned} V_0 \sin \omega t &= RI(t) + L_0(1 + A_V V_0^2 + B_V V_0^4 + \dots) \frac{dI}{dt} \\ &= RI(t) + L_V(V_0) \frac{dI}{dt}. \end{aligned} \quad (\text{S4})$$

Note that in Eq. (S4), the coefficient of dI/dt , $L_V(V_0)$, is constant during the time evolution of the system, and thus, the profile of $I(t)$ can be easily deduced from the knowledge of dynamic systems [21]. The numerical results are displayed in Figs. S2(a) and (b). For clarity, here, we chose a simplified parameter set: $V_0 = 1, \omega = 1, R = 10, I(0) = 0$, and $L_V(V_0) = +5$ [Fig. S2(a)] or -5 [Fig. S2(b)]. Note that the qualitative behavior of the solution depends only on whether the coefficient of dI/dt is positive or negative, and we

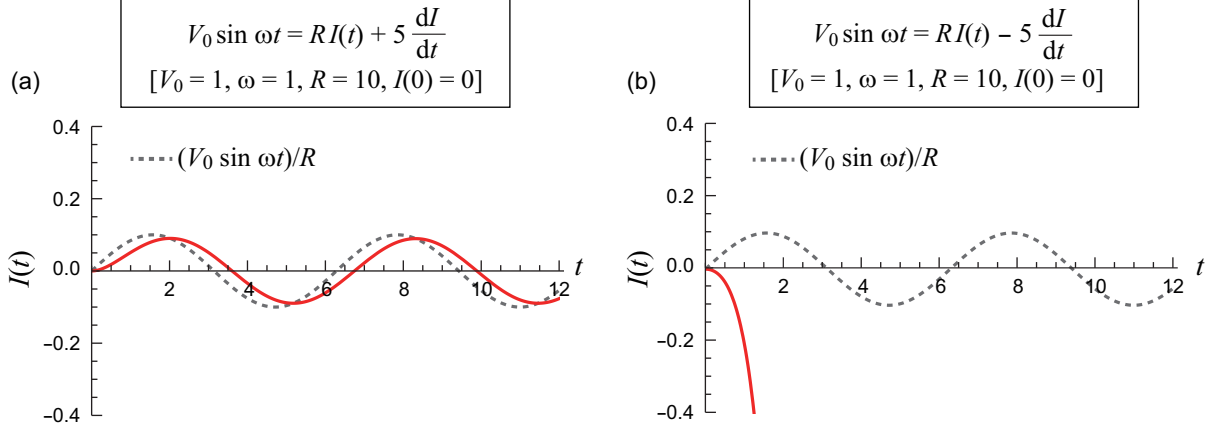


Fig. S 2. Time evolution of the current in the differential equation, Eq. (S4), for the case of positive inductance, $L_V(V_0) = +5$ (a) and negative inductance, $L_V(V_0) = -5$ (b).

chose parameters such that the characteristics of $I(t)$ can be clearly observed. Figure S2(a) shows the result for the case of $L_V(V_0) = +5$. When the coefficient of dI/dt is positive, the focus, $I_0(t) = (V_0 \sin \omega t)/R$ (denoted by the dotted line), is a stable focus (but time dependent due to the AC driving force, $V_0 \sin \omega t$); thus, $I(t)$ tracks the time-varying focus, with a finite delay. Figure S2(b) shows the case of $L_V(V_0) = -5$. When the coefficient is negative, the focus is unstable, and thus, $I(t)$ tends to separate from it over time. As a result, once $I(t)$ deviates from the focus by an infinitesimal amount, the deviation is unlimitedly amplified and diverges. Thus, a constant negative inductance makes the system unstable. This divergence instability is a natural consequence of the fact that the energy of the inductor, $\frac{1}{2}L_V(V_0)I^2$, diverges to negative infinity by increasing $|I|$ under constant negative inductance $L_V(V_0)$.

We next consider the main issue, Eq. (S3), which is a more nontrivial circuit equation in the sense that the coefficient of dI/dt varies during the time evolution. We set positive L_0 ($= 0.3$) so that the system is stable in the linear response. By choosing appropriate A and B, Eq. (S3) represents a nontrivial situation such that the coefficient of dI/dt changes its sign from positive to negative when the current becomes sufficiently large. Note that Eq. (S3) can be rewritten as $dI/dt = (V_0 \sin \omega t - RI)/[L_0(1 + AI^2 + BI^4)]$, and thus, it shows singularity the moment $L_0(1 + AI^2 + BI^4)$ reaches zero. To numerically solve Eq. (S3), we therefore introduce d^2I/dt^2 with an infinitesimally small positive coefficient, Γ ($= 10^{-8}$ in the present numerical calculation), which is just for the sake of the stability of the numerical tracking

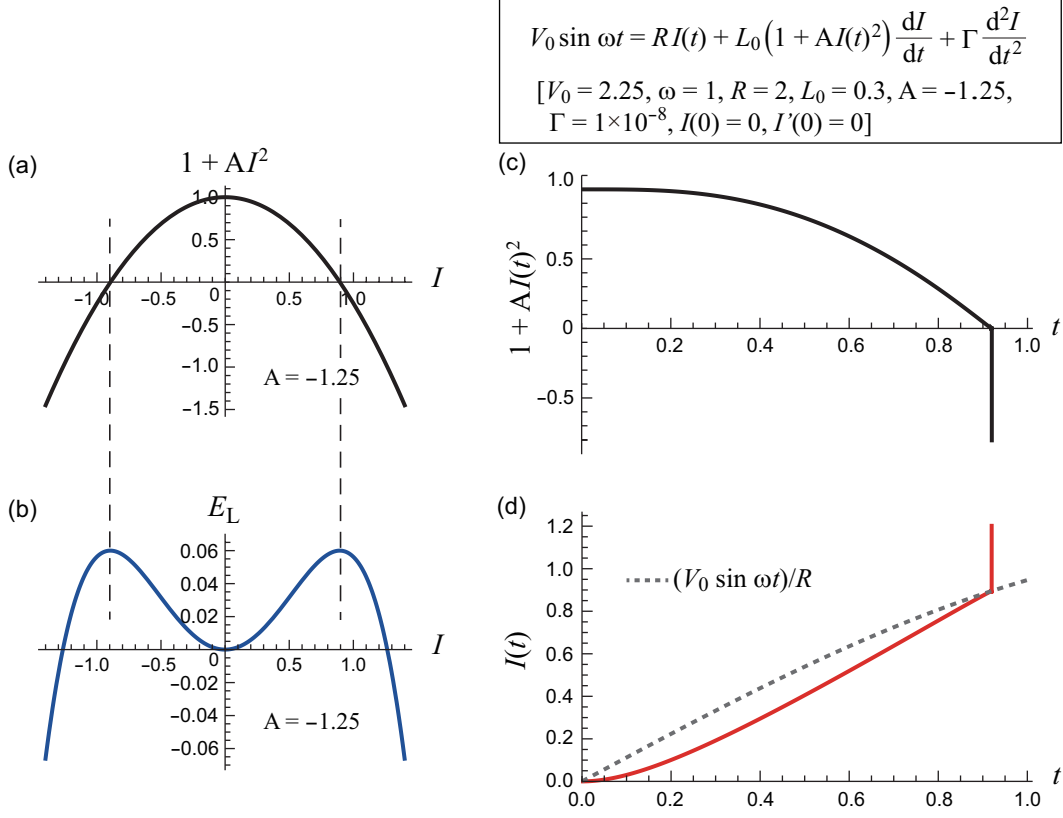


Fig. S 3. Time evolution of the current in the differential equation, Eq. (S5) with $B = 0$. (a, b) The coefficient of dI/dt (divided by L_0) (a) and the energy stored in the inductor (b) as a function of current. (c, d) Time evolutions of the coefficient of dI/dt (c) and current (d).

of the solution and is not important in the following discussion. Namely, the differential equation actually computed in this Supplemental Material is:

$$V_0 \sin \omega t = RI(t) + L_0(1 + AI(t)^2 + BI(t)^4) \frac{dI}{dt} + \Gamma \frac{d^2I}{dt^2}. \quad (\text{S5})$$

When considering real systems, it is also natural to assume that $I(t)$ is always first-order differentiable (i.e., dI/dt is always finite), and it therefore makes sense to consider such a second-order derivative term to ensure first-order differentiability.

First, we consider the case in which $A = -1.25$ and $B = 0$; thus, the coefficient of dI/dt and E_L depend on $|I|$, as shown in Figs. S3(a) and (b), respectively. The coefficient of dI/dt and dE_L/dI reach zero at $I \approx \pm 0.9$. Figures S3(c) and (d) show the numerical results in the nonlinear regime such that the coefficient of dI/dt reaches zero: the parameter set used is: $V_0 = 2.25, \omega = 1, R = 2, L_0 = 0.3, \Gamma = 1 \times 10^{-8}, I(0) = 0$, and $I'(0) = 0$. As the current increases with time, the coefficient of dI/dt decreases and eventually reaches

zero at $t \approx 0.92$ [Fig. S3(c)]. Concomitantly, $dI/dt \approx (V_0 \sin \omega t - RI)/[L_0(1 + AI^2 + BI^4)]$ diverges approximately positively so that the current catches up with the time-varying focus, $I_0(t) = (V_0 \sin \omega t)/R$, from below and overshoots it [Fig. S3(d)]. This upwards overshoot causes the coefficient of dI/dt to become negative [Fig. S3(c)], which never reverts to a positive value. Thus, the time-varying focus is unstable for $t > 0.92$, and accordingly, the current continues to separate from it and eventually diverges, similar to the case of Fig. S2(b). Thus, the system is unstable for a large V_0 . This behavior reflects the fact that in the absence of the I^4 term in Eq. (S5), the inductor energy can be unlimitedly decreased by increasing $|I|$ when the current exceeds the threshold value, $|I| \approx 0.9$ [Fig. S3(b)].

Next, we consider the case in which $A = -1.25$ and $B = 0.3$; i.e., the I^4 term with a positive coefficient is present in Eq. (S5). Thus, as $|I|$ increases, the coefficient of dI/dt first changes from positive to negative and then back to positive again [Fig. S4(a)]; furthermore,

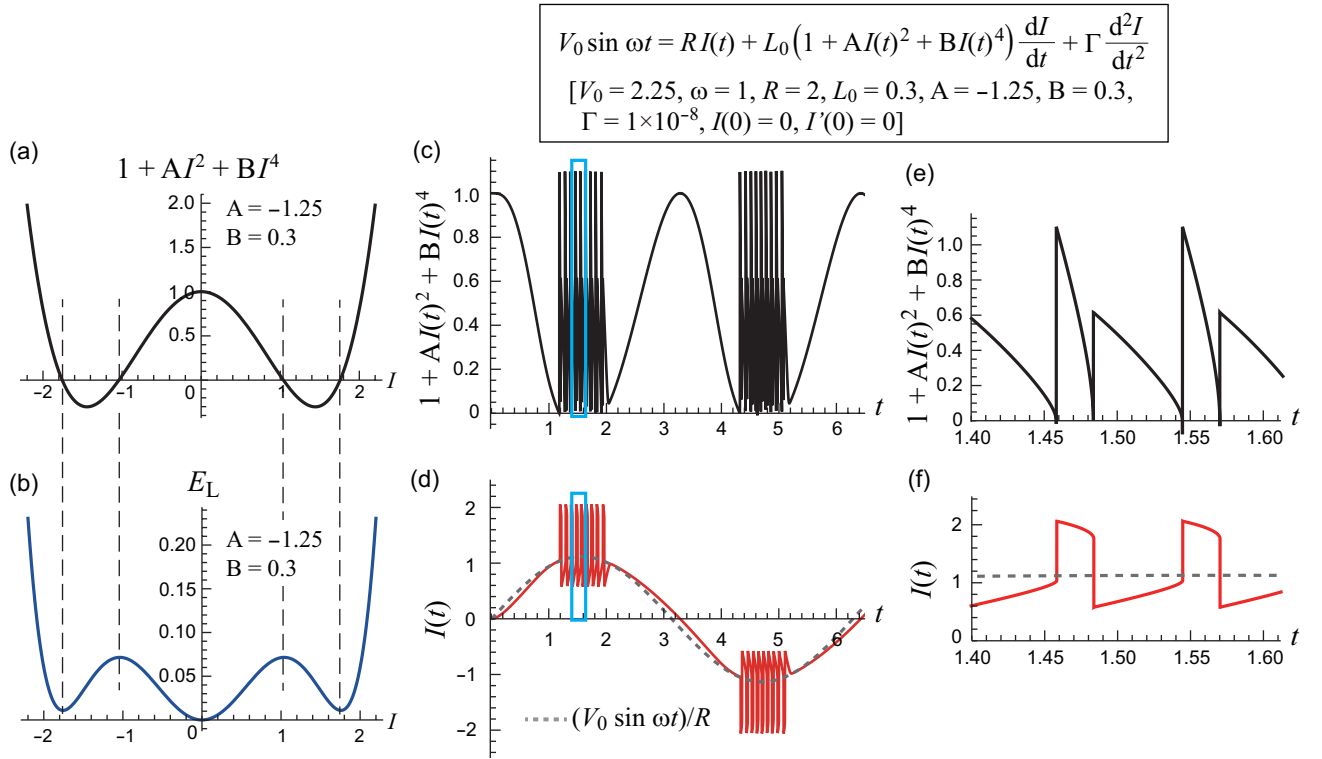


Fig. S 4. Time evolution of the current in the differential equation, Eq. (S5) with positive B. (a, b) The coefficient of dI/dt (divided by L_0) (a) and the energy stored in the inductor (b) as a function of current. (c, d) Time evolutions of the coefficient of dI/dt (c) and current (d). (e, f) Enlarged view of the squared area in panel (c) and (d), respectively.

for this parameter choice, the inductor energy is always positive for arbitrarily chosen I [Fig. S4(b)]. These features imply that the simultaneous divergence of I and the coefficient of dI/dt , as observed in Figs. S3(c) and (d), does not occur. Figures S4(c) and (d) show the numerical results in the nonlinear regime such that the coefficient of dI/dt reaches zero: the parameter set used is: $V_0 = 2.25, \omega = 1, R = 2, L_0 = 0.3, \Gamma = 1 \times 10^{-8}, I(0) = 0$, and $I'(0) = 0$. When the coefficient of dI/dt decreases from positive to zero, the system starts to oscillate [see also Figs. S4(e) and (f), which are magnified views of Figs. S4(c) and (d) during oscillation, respectively]. This oscillating behavior can be understood by considering the time evolution of Eq. (S5) in steps as follows. Whenever the coefficient of dI/dt reaches zero, the current tends to quickly catch up with the focus, $I_0(t) = (V_0 \sin \omega t)/R$, overshoot it upwards from below (or downwards from above), and diverge while $1 + AI^2 + BI^4 < 0$ (i.e., $1 < |I| < 1.75$); however, when the current falls outside this range, the coefficient of dI/dt becomes positive again [Fig. S4(a)]; thus, unlike in the case of $B = 0$ [Figs. S3(c) and (d)], the divergence of the current is halted, and the tracking towards the focus from above (or from below) restarts, resulting in decreasing (or increasing) current; during this tracking, the coefficient of dI/dt decreases and reaches zero again. In this way, a jerky oscillation of the current is achieved around the time-varying focus [Figs. S4(d) and (f)] when the current value results in a negative coefficient of dI/dt , exemplifying the unstable nature inherent to a negative coefficient of dI/dt .

In summary, numerical examinations have demonstrated that the hallmark of a negative coefficient of dI/dt is instability, such as divergence or spontaneous oscillation, and this phenomenon is never observed as an impedance with negative reactance. As would be best demonstrated by connecting a DC-voltage source of appropriate magnitude, an element that has a negative coefficient of dI/dt in a certain current range will operate as an oscillator [Figs. S5(a)–(c)]. Therefore, the experimental observation, $\text{Im}[\mathcal{V}_s^{1\omega}(\omega)/\mathcal{I}^{1\omega}(\omega)] \approx -|\eta|\omega$, in the nonlinear regime should be considered beyond the framework of Eqs. (S1)–(S3). As discussed in the main text, we consider this issue in terms of time-varying Joule heating and its impact on the AC electrical response.

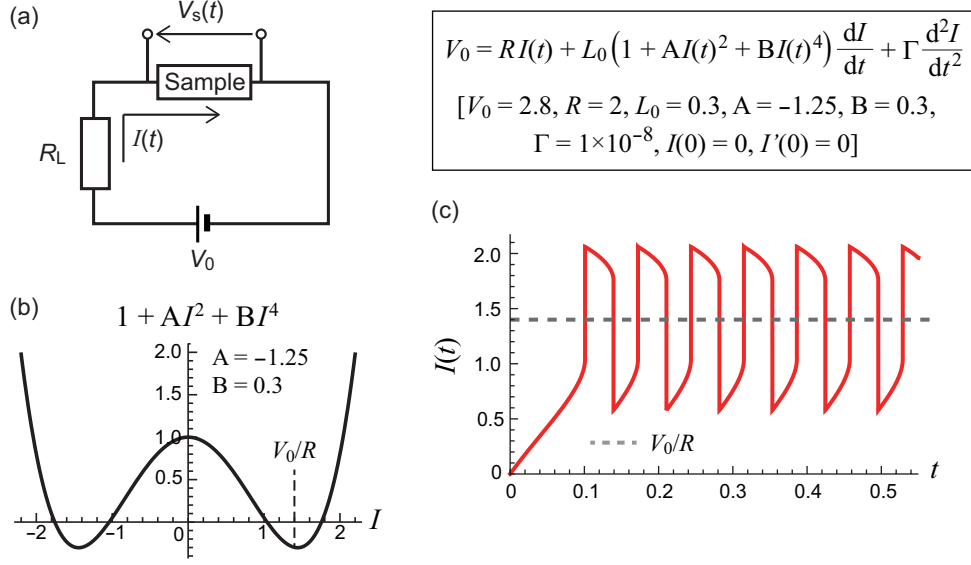


Fig. S 5. Oscillator function of an element that shows a negative coefficient of dI/dt under the application of a DC-voltage of appropriate magnitude. (a) Experimental circuit for the demonstration of the oscillator function. (b) The coefficient of dI/dt (divided by L_0) as a function of current. The broken line indicates a condition of V_0 and R that show the oscillator function. (c) Time evolution of the self-sustained current oscillation in the differential equation, Eq. (S5) with positive B .